LA-UR-23-29157

Approved for public release; distribution is unlimited.

Title:	Development of Mechanistic Fission Gas Release and Swelling Models for UN Fuels in BISON
Author(s):	Rizk, Jason Tyler Schneider, Anton Jacques Cooper, Michael William Donald Andersson, Anders David Ragnar Matthews, Christopher
Intended for:	Report
Issued:	2024-12-17 (rev.1)

Development of Mechanistic Fission Gas Release and Swelling Models for UN Fuels in BISON

Jason Rizk, Anton Schneider, Michael Cooper, David Andersson, and Christopher Matthews

Los Alamos National Laboratory

July 2023

Contents

1 Executive Summary

This report describes the work in NEAMS (Nuclear Energy Advanced Modeling and Simulation) to develop a mechanistic fission gas model for uranium nitride fuels in BISON. The existing Sifgrs (Simple integrated fission gas release and swelling) model tracks the average properties of two bubble populations in the bulk and at the grain boundaries. It was recognized that dislocations play a crucial role in the fission gas swelling of UN, and an irradiation-induced dislocation density model was needed, as well as a model describing how fission gas interacts with dislocations creating a third population of bubbles along dislocations.

A mechanistic model that tracks dislocation bubbles was implemented in Sifgrs. This model was used to simulate fission gas swelling and release in UN. Lower-length-scale calculations and experimental observations from carbide fuel were leveraged to help populate the model with essential parameters. As a placeholder, an empirical function was formulated for the evolution of the dislocation network. Because of the difference in evolution of this network at different temperatures, the dislocation bubbles are able to capture behavior that the bulk intragranular bubbles cannot. It was found that the bulk bubbles dominate microscopic swelling at low temperatures, and the dislocation bubbles dominate at higher temperatures. Based on this model, the transition between the two bubble types is the main factor behind the breakaway swelling phenomenon in UN. In order to test the model, a couple of assessments were run. For the lower temperature JOYO pins, the model produces reasonable fission gas release and swelling values. For the higher temperature SP1 pin, the model dramatically underestimates the fission gas release. This issue is attributed to the gas being trapped inside dislocation bubbles, unable to escape to grain boundaries to cause fission gas release, and could be remedied by a mechanistic dislocation model that allows the dislocation density to decrease at very high temperatures.

A preliminary mechanistic dislocation model was developed supported by first-principle calculations. These calculations provided valuable insight into how interstitial defects cluster in UN in the $\{110\}$ orientation, and may eventually form dislocation loops, leading to the conclusion that dislocation loops may nucleate from these clusters. An estimate of the dislocation line energy in UN was obtained and will be improved in future work. The free-energy cluster dynamics code Centipede was used to track interstitial and vacancy absorption at dislocation loops and calculate their growth. In addition, improvements to Centipede were made including new convergence criteria for transient simulations and sink driving force updates.

2 Introduction

Many of the required models to capture the fuel performance of uranium nitride – thermal conductivity, elastic moduli, creep, etc. – have been implemented in BISON in previous years. One of the last remaining pieces is a model that mechanistically describes the response of the fuel to evoloving temperature and fission rate profiles. In order to provide a placeholder for a more accurate fission gas swelling and release model, the model utilized in the European code TRANSURANUS was implemented, along with a temperature correction to make the model applicable to nitride fuels [1]. In addition, a simplified fission gas release model was implemented [2]. While these models provide placeholders for more representative models, they are extremely limited in applicability in uranium nitride fuel. In order to enable the qualitative assessment of BISON UN fuel performance simulations, an improved fission gas swelling and release model is needed to be able to utilized all of the sparse irradiation data available for this advanced fuel.

Fission gas models for ceramic nuclear fuel fission gas swelling and release typically consider two populations of bubbles, the bulk intragranular bubbles and the intergranular bubbles [3]. The intragranular bubbles form and accumulate inside the grain, and act to slow the migration of gas atoms to the grain boundary. At the same time, fission fragments in the fuel knockout gas atoms from the bubbles, resulting in a pseudo-steady-state concentration of diffusing fission gas in the lattice. The intergranular bubbles absorb gas that eventually reaches the grain boundaries, leading to interconnection once a grain-face saturation threshold is reached. Once this network of the interconnected bubbles reach a free surface, the contents of the high-pressure bubbles flows into the plenum, resulting in a build up in pressure on the inside surface of the cladding. In addition to fission gas release, both grain-interior and grain-face bubbles cause significant swelling of the fuel, which leads to pellet-cladding interaction (PCI).

While the general behavior of fission gas in uranium nitride (UN) and uranium carbide (UC) fuel is similar to UO_2 – swelling due to fission gas bubbles in inter- and intra-granular bubbles, and percolation of grain-face bubbles resulting in fission gas release – these advanced ceramic fuels have a markedly different swelling trend. This so-called "break-away" swelling has yet to be captured in fuel performance models in a robust manner. Early efforts of implementing the BISON UO_2 standard fission gas model, Sifgrs, failed to capture this more complex swelling behavior. Leveraging some early work on dislocation-bubble interaction in UO_2 [4, 5], adaptation of Sifgrs focused on incorporation of a third population of bubble, the intragranular dislocation bubble. Experimental evidence that fission gas interacts with dislocations has existed for decades [6–8], and has even been suggested as nucleation sites for bubbles [9].

By building on models developed for fission gas behavior in UO_2, especially the complexity introduced by new dislocation bubbles [4, 5] we have created a new fission gas swelling and release model for UN. This model required a number of enhancements to the base Sifgrs model to be able to incorporate the various material specific properties required to capture fis-

sion gas behavior. Many of these complexities have been started in previous years [10], with the modifications relevant to dislocations as a primary focus for this work. Lower-length scale computations on fundamental material properties (e.g., diffusivities) has been fit to analytical expressions and incorporated into this new model. Such details are important to capture a true mechanistic response of some of these parameters. This new model has been implemented in BISON and exercised against a subset of experimental data and integral pin simulations. While not fully complete, this model is mature enough to support the claim that dislocations play a significant role in the break-away swelling and overall fission gas behavior in UN.

Following early successes in the BISON UN fission gas model, it was clear that the growth of dislocations needed to be captured mechanistically rather than relying only on fits to limited experimental data. To this end, Centipede has been extended to capture dislocations in transient simulations of point defects in irradiated UN fuel. This required a number of changes to the standard Centipede convergence criterion, defect sink evolution, and a number of Centipede code changes to enable the tracking of this new type of defect. With these new changes in place, this initial dislocation model captures some the expected behavior of dislocations. A number of changes are still required – primarily in the nucleation and network growth behavior – but these initial simulations show promise in mechanistically capturing the behavior of dislocations and other defects as a function of temperature, irradiation, and chemistry.

What follows is a description of 1) the BISON UN fission gas swelling and release model with comparison to a limited data set, and 2) introduction of a new dislocation model in Centipede. Details on assumptions, model strengths and weaknesses, and future work is included for both thrusts. Rapidly following this report, the models in both Centipede and BISON need to be refined, and likely coupled in a manner so information can flow between the two codes. Following this, application to a number of integral assessment cases will be the true test of the new model, culminating in completion of a "baseline" capability of BISON for UN fuel performance.

3 UN Fission Gas Model

Building on efforts from the previous year, a more refined fission gas release and swelling model as been developed based on the BISON Sifgrs model [11]. In preparation for this new model, a major clean-up effort of the fission gas section of the BISON code was performed. Although the details of such refactoring will not be accounted for here, the refactoring, reorganizing, and deployment by both Idaho National Laboratory and Los Alamos National Laboratory developers have made the Sifgrs model in BISON much more accessible. This primarily consisted of splitting the physical models describing fission gas behavior into a base class, while separating material parameters into separate fuel specific classes. The refactoring of the Sifgrs model helped give it a necessary improvement in clarity and made new models much easier to implement. These changes not only make future model implementation faster, but also help avoid mistakes when implementing or using the models due to the improved clarity.

Fission gas is known to interact with the dislocation network in ceramic fuel [6–8]. The dislocation lines act as nucleation sites for bubbles to form, help to trap gas atoms, and provide pipe diffusion pathways to funnel the gas atoms to the bubbles [5, 9]. Fig. 3.1 illustrates the three types bubbles, and the color scheme of green for bulk intragranular bubbles, yellow for intragranular dislocation bubbles, and orange for grain face bubbles, is maintained throughout the figures in this chapter. In the model, dislocation bubble nucleate along dislocation lines by a constant factor per unit length. They absorb gas atoms and vacancies both at the bubble periphery and along the dislocation lines. Like the bulk intragranular bubbles, they undergo resolution of gas atoms from the bubble back into the matrix. And like intergranular bubbles, they can coalesce as they become large. By these mechanisms, dislocation bubbles adopt properties similar to both the bulk bubbles and the grain boundary bubbles.

Preliminary efforts on capturing the behavior of UN indicated dislocation bubbles likely have a role to play in capturing the breakaway swelling behavior of the fuel. As part of the implementation of UNSifgrs, the dislocation bubble model described in [4], originally meant for bubble coarsening in UO_2 under transient conditions, was expanded to UN. A thorough description of the model is given here in the following sections. In this chapter, the fission gas behavior of nitride and carbide fuels that motivates this work is reviewed. A solid and Cs swelling relation is given that sums with the fission gas swelling to give total swelling. Fits to the diffusion of relevant defects calculated using Centipede are presented. The dislocation bubble model is described. Bubble overpressurization and dislocation punching is investigated. An empirical dislocation density function is created for UN to help calculate intragranular swelling, which is then compared with experimental measurements. The UN Sifgrs model including dislocation bubbles is tested using fuel pin assessment cases.

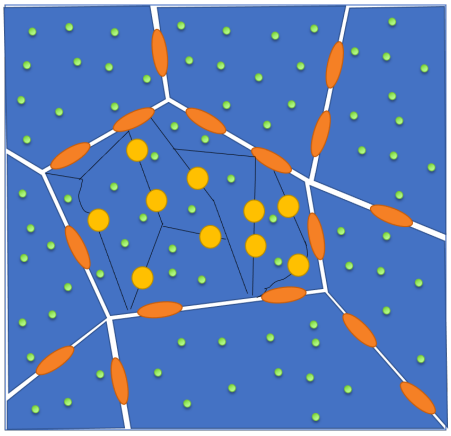

Figure 3.1: Illustration showing the three types of bubbles: intragranular bulk (green), intragranular dislocation (yellow), and intergranular (orange).

3.1 Overview of Fission Gas Behavior in Nitride and Carbide Fuels

The notable swelling behavior of carbide and nitride fuels was reviewed in a previous report [10], and is summarized here for reference.

In order to understand the three swelling regimes, it is helpful to use definitions based on empirical observations of fission gas bubbles [9, 12]. Bubbles have been categorized into three populations [12]. The first, P_1, consists of small intragranular bubbles with sizes less than 30 nm. These are typically observed in the low temperature region near the cladding. Moving inward towards the fuel center where temperatures are greater, larger intragranular bubbles form population P_2. The size of the P_2 bubbles ranges from 30 to 400 nm. The population P_2 becomes significant where the temperature exceeds the threshold temperature T_2, which corresponds with an increase in the microscopic, or intragranular, swelling. Bubbles along the grain boundaries form P_3, which are larger than 40 nm. While P_3 bubbles exist at temperatures below T_2, they become more significant when temperatures exceed T_2. The last threshold temperature T_3 corresponds to a decrease in microscopic swelling that occurs in the center of the fuel pin, and is associated with the interconnection of P_3 bubbles in conjunction with the mechanical weakening and fracture of the grain boundaries [13] causing a significant release of fission gas.

The rate of intragranular swelling in nitride fuel has been shown to increase for temperatures greater than a threshold temperature [9,12,14]. This phenomenon, termed "breakaway swelling," needs to be understood and quantified because it presents large uncertainty and may pose a significant risk to the cladding. Breakaway swelling is associated with the formation of large intragranular bubbles (between 30 and 400 nm) [12]. Fig. 3.2 shows the change in swelling rate with temperature after the threshold temperature is reached in carbide fuel (MC) for two values of burnup. At even greater temperatures, the rate of swelling decreases with temperature after a second threshold temperature is reached. This second threshold is associated with the growth and interconnection of intergranular bubbles, typically larger than 40 nm [12], indicating that a larger fraction of gas is exiting the grain and reaching the grain boundaries at those higher temperatures.

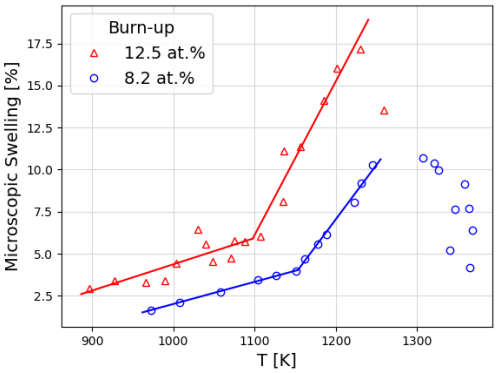

Figure 3.2: Microscopic swelling in MC as a function of temperature depicting "breakaway swelling" at two different burnup values [12].

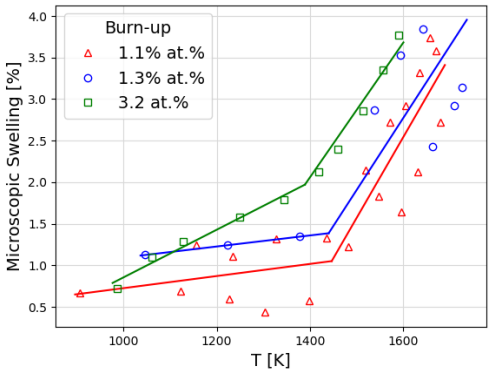

Figure 3.3: Microscopic swelling in MN as a function of temperature depicting "breakaway swelling" at two different burnup values [14].

The threshold temperature for breakaway swelling is known to depend on burnup and chemistry. Similar to Fig. 3.2, Fig. 3.3 shows the microscopic swelling vs. temperature for MN, with a smaller range of burnup values. Fig. 3.4 shows the same but for mixed carbide-nitride fuel. The transition temperature decreases with greater burnup and increases with greater nitride content, with MN having a much greater threshold for breakaway swelling than MC. Fig. 3.5 shows the transition temperature as function of burnup for various contents of carbide and nitride. The transition temperature follows an inverse power law dependence on burnup for the different compositions of $MC_{1-x}N_x$ fuel. The curve shifts up in temperature linearly with increasing nitride content, with MN having a transition temperature that is 200 K greater than that of carbide fuels for all values of burnup.

Dislocations may aid to explain the breakaway swelling phenomenon via two mechanisms. The first is the decrease in point defect concentration, particularly the concentration of interstitials, due to the formation of dislocation networks which act as sinks for interstitials. With a

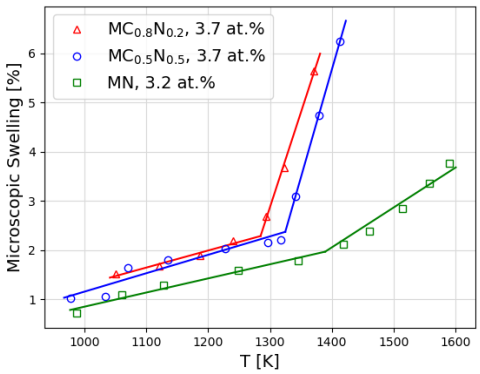

Figure 3.4: Microscopic swelling in MCN as a function of temperature depicting "breakaway swelling" with three different compositions [12, 14].

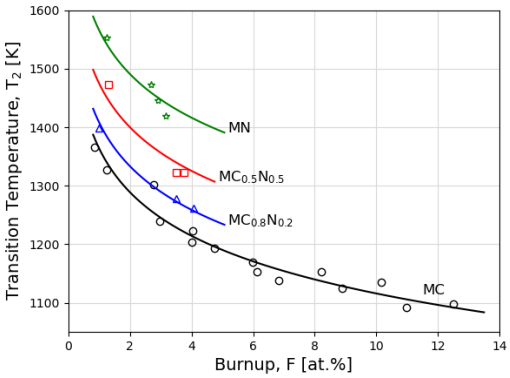

Figure 3.5: T_2 transition temperature that signifies breakaway swelling in UC and UN fuels.

lower concentration of interstitial point defects, bubbles are able to absorb more net vacancies and grow at an increased rate. The second mechanism, supported by this work, is the interaction of fission gas with dislocations to form dislocation bubbles. Both theories rely on the temperature and burnup dependence of the dislocation network density to be somewhat similar to that of breakaway swelling, where the dislocation density increases sharply at a similar transition temperature.

3.2 Solid and Cs Swelling

Part of microscopic swelling is the formation of solid fission products and cesium. In general, the amount of solid fission product swelling can be estimated to be about 0.5% per at.% burnup overall based on experimental data [12, 15]. However, in the periphery of the pellets near the cladding where swelling due to fission gas is low, the swelling rate due to solid fission products reaches 1.5% swelling per % FIMA. In BISON, the solid swelling and the fission gas swelling contribute independently to the total swelling. Therefore, the solid swelling value without fission gas swelling is implemented, given by,

$$\left(\frac{\Delta V}{V}\right)_{solid} = 1.5 \cdot F, \tag{3.1}$$

where F is the burnup in FIMA.

3.3 Diffusion

As with all mechanistic fission gas swelling and release models, diffusion of defects is at the heart of the Sifgrs model. In order to capture the temperature and fission rate dependent diffusivity of point defects, cluster dynamics codes are typically required. Centipede is one such cluster dynamics code that utilizes free-energy cluster dynamics (FECD) simulations informed by lower length scale (LLS) simulations to estimate the irradiation enhanced self- and xenon diffusivity in a variety of fuels [16–19]. In order to capture an accurate representation of fission gas diffusivity in BISON, several fits have been developed to distill and utilize the relevant lower-length scale informed material properties into BISON. What follows is a short discussion of the different relevant regimes and how the analytial fit was developed and implemented in BISON.

Diffusion in materials under irradiation is expected to exhibit the three temperature regimes seen in irradiated nuclear fuel. The three regimes are:

- D_1: intrinsic diffusion at high temperatures
- D_2: irradiation-enhanced diffusion at intermediate temperatures
- D_3: athermal irradiation-induced diffusion at low temperatures

D_1 is the diffusion that occurs when defects are at thermal equilibrium concentrations, and is dependent only on temperature. Likewise, D_2 is temperature dependent, but is elevated by enhanced concentrations of defects caused by irradiation. D_2 is dependent on temperature, and

exhibits a square-root dependence with fission rate [20]. D_3 is strictly due to irradiation-induced atomic mixing in damage cascades [20, 21], is athermal, and is linearly dependent on fission rate. D_1 can be computed directly from the defect energies obtained from DFT and MD, while D_2 must use cluster dynamic simulations. D_3 can be calculated using molecular dynamics (MD) simulations of irradiation damage cascades for materials like UN that have high electronic heat transfer to dissipate the energy of a thermal spike [18, 22]. D_3 is typically only applied to non-bulk defects such as xenon and is not utilized for self defects, meaning self-interstitials, vacancies, antisites, and the corresponding clusters.

The total diffusivity of a defect is given by:

$$D_{defect} = D_1 + D_2 + D_3 \tag{3.2}$$

While thermal equilibrium diffusivity is fit using a simple Arrhenius relation,

$$D_1 = D_1^0 \exp\left(-\frac{Q_1}{k_B T}\right), \tag{3.3}$$

D_2 is fit using the exponential of a cubic polynomial of reciprocal temperature due to its more complex shape (see Fig. 3.7). The fission rate density dependence takes a square root relation.

$$D_2 = \sqrt{\dot{F}} \sum_i \left[A_{2_i}^0 \exp\left(-\frac{Q_{2_i}^{\{1\}}}{k_B T} - \frac{Q_{2_i}^{\{2\}}}{(k_B T)^2} - \frac{Q_{2_i}^{\{3\}}}{(k_B T)^3} \right) \right]. \tag{3.4}$$

D_3 is assumed to increase linearly with the fission rate density.

$$D_3 = A_3^0 \dot{F} \tag{3.5}$$

Centipede includes a dependence on the partial pressure of N_2 gas in order to be able to compare calculations more directly with experiments where the N_2 partial pressure was characterized. The partial pressures must be selected such that UN is stable. Fig. 3.6 shows the stability region of UN as a function of temperature and partial pressure. Calculations were performed at partial pressure values along the dotted line along the middle of the UN region, which is given by an Arrhenius relation [23]:

$$p_{N_2}^{middle}\ [\text{atm}] = 6.48 \cdot 10^9 \exp\left(\frac{-4.46\ \text{eV}}{k_B T}\right). \tag{3.6}$$

3.4 Dislocation Bubble Model

The model for intragranular bubble growth and evolution makes the simplifying assumption of an average bubble size, R [m], and an average bubble concentration, N [m^{-3}], for the two bubble types, bulk (subscripted with 'b') and dislocation (subscripted with 'd') [4, 24, 25]. This

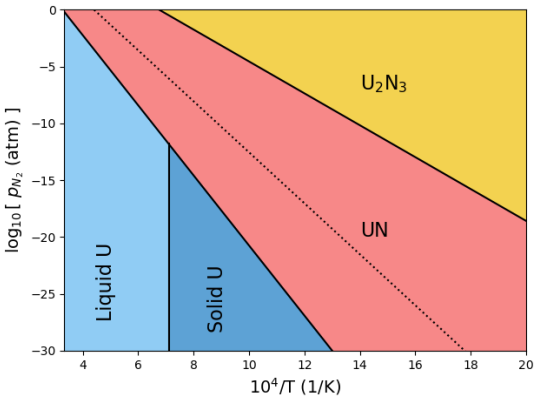

Figure 3.6: Phase diagram of UN with the partial pressure of N_2 gas vs reciprocal temperature. The diffusivity calculations in Centipede were performed at partial pressure values shown by the dotted line.

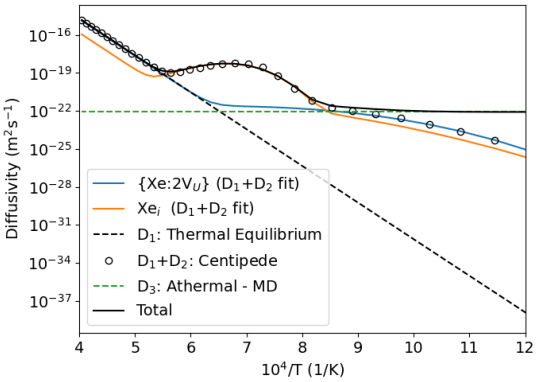

Figure 3.7: Fit of diffusivity for Xe. The two dominant contributions to total diffusivity from $\{\text{Xe:2V}_U\}$ and Xe_i are shown, as well as the contribution from athermal (D_3) diffusion calculated using MD. The fission rate density ($\dot{F}$) is 10^{19} fissions m^{-3} sec^{-1}.

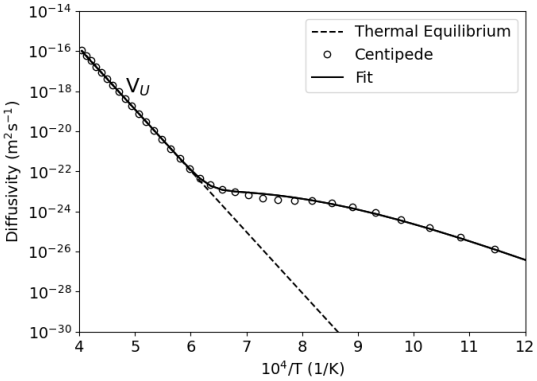

Figure 3.8: Fit of diffusivity for U vacancies.

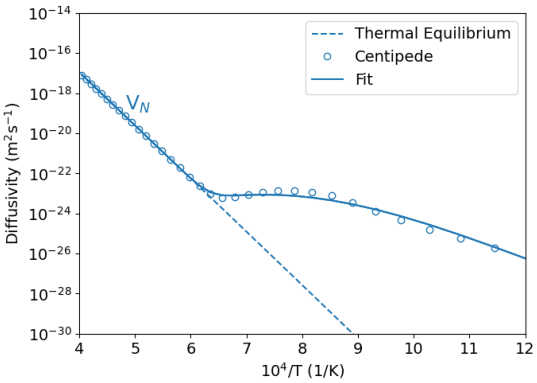

Figure 3.9: Fit of diffusivity for N vacancies.

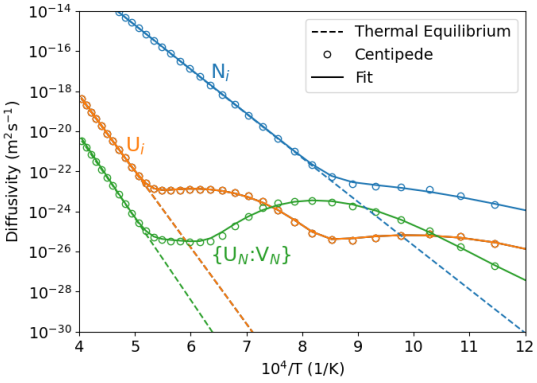

Figure 3.10: Fit of diffusivity for U interstitials, N interstitials, and $\{U_N{:}V_N\}$.

Table 3.1: Diffusion Equation Parameters (Eqs. (3.3) to (3.5)).

Defect	D_1^0	Q_1	$A_{2_0}^0$	$Q_{2_0}^{\{1\}}$	$Q_{2_0}^{\{2\}}$	$Q_{2_0}^{\{3\}}$	$A_{2_1}^0$	$Q_{2_1}^{\{1\}}$	$Q_{2_1}^{\{2\}}$	$Q_{2_1}^{\{3\}}$	A_3^0
Xe_i	$6.12{\cdot}10^{-5}$	5.76	$3.40{\cdot}10^{-12}$	27.67	-5.28	0.302	$1.45{\cdot}10^{-33}$	-1.80	0.156	0	$8.2{\cdot}10^{-42}$
$\{Xe{:}V_U\}$	$7.54{\cdot}10^{-4}$	5.76	$2.06{\cdot}10^{-33}$	-0.408	-0.0798	0.00940	0	0	0	0	-
V_U	$2.11{\cdot}10^{-4}$	6.04	$8.12{\cdot}10^{-42}$	-6.01	0.543	-0.0124	0	0	0	0	-
V_N	$5.15{\cdot}10^{-7}$	5.28	$3.64{\cdot}10^{-51}$	-11.34	0.959	-0.0229	0	0	0	0	-
U_i	$1.17{\cdot}10^{-3}$	7.57	$6.70{\cdot}10^{-35}$	2.83	-1.06	0.0813	$6.81{\cdot}10^{-51}$	-6.19	0.269	0	-
$\{U_N{:}V_N\}$	$2.53{\cdot}10^{-4}$	8.22	$2.25{\cdot}10^{-47}$	-8.51	0.670	0	$6.88{\cdot}10^{-99}$	-39.08	3.25	-0.0837	-
N_i	$2.03{\cdot}10^{-4}$	4.37	$1.48{\cdot}10^{-12}$	-12.32	0.959	-0.0227	0	0	0	0	-

assumption allows for the bubble behavior to be expressed by five equations,

$$\frac{dN_b}{dt} = \nu_b - b_b \phi_b N_b, \tag{3.7}$$

$$\frac{dN_d}{dt} = \nu_d - b_d \phi_d N_d, \tag{3.8}$$

$$\frac{\partial c}{\partial t} = D\Delta^2 c - g_b N_b - (g_d + g')N_d + b_b m_b + b_d m_d + G - 2\nu_b - 2\nu_d, \tag{3.9}$$

$$\frac{\partial m_b}{\partial t} = 2\nu_b + g_b N_b - b_b m_b, \tag{3.10}$$

$$\frac{\partial m_d}{\partial t} = 2\nu_d + (g_d + g')N_d - b_d m_d, \tag{3.11}$$

where c [m^{-3}] is the concentration of gas atoms in the matrix, m [m^{-3}] is the concentration of gas atoms in the bubbles, ν [$m^{-3}s^{-1}$] is the nucleation rate given for dislocation bubbles by Eq. (3.13), b [s^{-1}] is the resolution rate given by Eq. (3.14), g_d [s^{-1}] is the trapping rate for dislocation bubbles given by Eq. (3.17), g_b [s^{-1}] is the trapping rate for bulk bubbles, and G [$m^{-3}s^{-1}$] is the generation rate of fission gas atoms. When calculating the number of bubbles, resolution destroys only the smallest bubbles with a size of two atoms. So the correction factor ϕ is applied, which is the fraction of dimers out of the total number of bubbles, estimated as,

$$\phi = \frac{1}{m-1}. \tag{3.12}$$

The following sections describe dislocation bubble nucleation, resolution, gas atom trapping, bubble growth, and bubble coalescence. Aspects of the model for dislocation bubbles are handled in a similar way to the bulk bubbles. Both the bulk intragranular bubbles and intergranular bubbles were described in the previous milestone report [10].

3.5 Dislocation Bubble Nucleation

Dislocation bubbles nucleate along new dislocation lines by a factor $K = 1 \cdot 10^6$ bubbles/m, which is the number of bubbles nucleated per dislocation line length. Nucleation is given by,

$$\nu_d = K\frac{d\rho_d}{dt}. \tag{3.13}$$

The value of K comes from previous modeling work for UO_2 [4], and from bubble density and dislocation density measurements in carbide fuel [6], where the bubble density was found to increase linearly with dislocation density by $1.2 \cdot 10^6$ bubbles/m at 1025 K. In the same experiment, bubbles were also found to nucleate on needle-shaped precipitates, and the bubble density also increased linearly with the needle line density by about $1.9 \cdot 10^6$ bubbles/m at both 1240 K and 1550 K, demonstrating no temperature-dependence of this nucleation factor. This can be seen by the slopes in Fig. 3.11. Only the intercepts at zero dislocation or needle line density changes as a function of temperature, which is interpreted as the concentration of the intragranular bubbles if no dislocations or needles were present.

Note that $N_d \neq K\rho_d$, because the number of dislocation bubbles nucleated on a fresh dislocation line may decrease over time due to both resolution and coalescence.

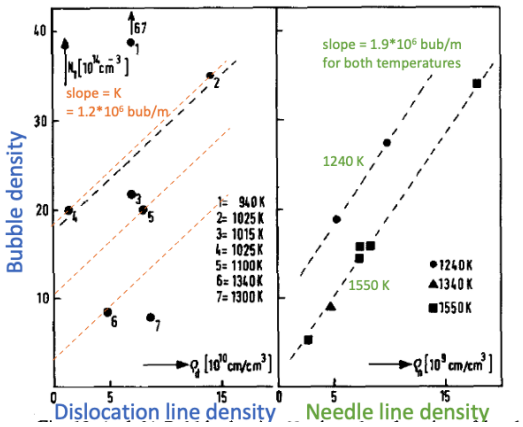

Figure 3.11: Illustration of the dislocation bubble nucleation factor in carbide fuel. Original figure from [6].

3.6 Resolution

Resolution was described in a previous milestone [10] for bulk intragranular bubbles, and is treated the same way for dislocation bubbles.

The resolution process in UN is treated using the homogeneous theory that assumes gas atoms in bubbles re-enter the lattice due to ballistic collisions with energetic fission fragments knocking them out of the bubble and into the lattice. This theory is preferred over the heterogeneous theory [26] for UN due to its quick energy transport properties (e.g., high thermal conductivity). The heterogeneous theory, appropriate for materials with lower thermal conductivity such as UO_2, assumes the fission product track creates a thermal spike that destroys bubbles within the track radius, causing the gas atoms to re-enter solution. The total homogeneous resolution rate is given by,

$$b\ [\mathrm{s}^{-1}] = \dot{F} \int b_0(R_b) n(R_b) \rho(R_b) dR_b, \tag{3.14}$$

where $\dot{F}$ [fp m^{-3}s^{-1}] is the fission rate density, R_b [m] is the bubble radius, b_0 [m^6 at^{-1} fp^{-1}] is the resolution parameter, n [at bl^{-1}] is the number of atoms in a bubble, and ρ [bl m^{-4}] is the bubble concentration distribution function, defined so that the total concentration of bubbles is given by,

$$N\ [\mathrm{m}^{-3}] = \int \rho(R_b) dR_b. \tag{3.15}$$

The resolution parameter b_0 can be thought of as the number of resolution events that occurs per atom density and per fission density.

Matthews et al. [27, 28] calculated the resolution parameter for carbide, silicide, and nitride fuel types using the Binary Collision Approximation code 3DOT. Fission fragments were randomly created in the material. The work calculated both ion-atom interactions and electronic stopping power. Electronic losses were found to be very significant, accounting for about 90 %

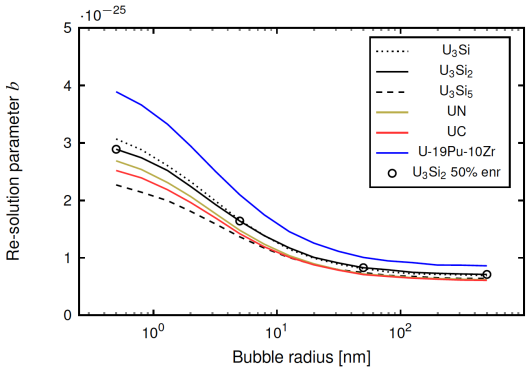

Figure 3.12: Re-solution parameters for several fuel types calculated using 3DOT simulations. Reproduced from [28].

of the original fission fragment energy. The resolution parameter was found to decrease as bubble radius increases up to about 50 nm, after which it remains roughly constant, as shown in Fig. 3.12. This dependence on bubble size is expected due to the interior of the bubble being protected from resolution by low-energy cascades that are slowed within larger bubbles [9].

Fig. 3.12 shows the resolution parameter as a function of bubble radius calculated by Matthews et al. [27, 28] for several fuel types including UN. In the model implemented for UN, the resolution parameter is a function of bubble radius,

$$b_0^{UN}(R_b) = 2.38 \cdot 10^{-25} \left(\frac{0.5 \cdot 10^{-9}}{R_b} \right)^{0.23} \text{[m}^6\text{]}. \tag{3.16}$$

3.7 Trapping

The trapping of gas atoms at bubbles is considered to be driven by diffusion of gas atoms within the interaction vicinity of the bubbles. The trapping rate is given by,

$$g_d \text{ [s}^{-1}\text{]} = 4\pi f_{tr} D^{fg} R, \tag{3.17}$$

where R [m] is the average radius of the bubbles. The nucleation factor f_{tr} is a calibration term equal to 1 or greater to account for an extended interaction distance between gas atoms and bubbles.

Gas can also trap and travel along dislocation line to reach dislocation bubbles. The trapping rate at dislocations is given by,

$$g' \text{ [s}^{-1}\text{]} = \frac{2\pi D_d^{fg} \rho_d}{\ln \frac{r_{ws,d}}{Z_d r_d} - \frac{3}{5}}, \tag{3.18}$$

where $r_{ws,d} = (\pi \rho_d)^{-1/2}$ [m] is the radius of the Wigner-Seitz cell associated with a dislocation, and r_d [m] is the dislocation core radius, which is roughly the length of the Burger's vector.

$Z_d = 5$ is a trapping radius factor to account for the elastic strain field around the dislocation core causing gas atoms to imminently absorb from greater distances. Trapping at dislocation bubbles is given as the sum of trapping at the bubbles and the dislocations, $g_d + g'$. This formulation should be updated to exclude the fraction of the dislocation line covered by the dislocation bubbles, because the part of the dislocation line that is covered by a bubble that already traps gas at its surface cannot also contribute to gas trapping. If a large fraction of the dislocation line is covered, discussed in Section 3.11.2, then that fraction is contributing nonphysically to the trapping by what may be a non-negligible amount.

3.8 Dislocation Bubble Radii

The PolyPole-2 algorithm [11] briefly described in Section 3.10 supplies the average number of atoms per bubble m and the diffusion rate of gas atoms to the grain boundaries. The number densities of the bulk bubbles N_b and dislocation bubbles N_d are then calculated by the `BubbleEvolution` and `CoarsenedBubbleEvolution` methods, respectively.

The calculation of bubble size and swelling is performed based on a physics-based approach previously used for UO_2 and U_3Si_2 that considers both gas atoms and vacancies being absorbed at bubbles [25]. The intragranular bubbles are assumed to be spherical. The equilibrium pressure p_{eq} [Pa] of the bubbles can be calculated using the Young-Laplace equation,

$$p_{eq} = \frac{2\gamma}{R} - \sigma_h, \tag{3.19}$$

where σ_h [Pa] is the hydrostatic stress. The surface energy for UN is estimated to be $\gamma = 1.74 \pm 0.76$ [Jm^{-2}] based on DFT calculations from the literature [29, 30].

The actual pressure inside the bubbles is calculated following the van der Waals equation of state and is given by,

$$p = \frac{k_B T \eta}{\Omega}, \tag{3.20}$$

where $\eta = m/(N n_{iv})$ is the average number of gas atoms contained vacancy volume, and $\Omega = 1.17 \cdot 10^{-28}$ m^3 is the vacancy volume in UN. n_{iv} is the number of vacancies per intragranular bubble, caluculated by

$$\frac{dn_{iv}}{dt} = \frac{2\pi D_d^v \delta}{kT\zeta}(p - p_{eq}), \tag{3.21}$$

where D_d^v[$\mathrm{m}^2\mathrm{s}^{-1}$] is the vacancy diffusion coefficient along dislocations, δ[m]$= (4/3\pi N_d)^{-1/3}$ is the radius of the Wigner-Seitz cell for a dislocation bubble, and ζ is a dimensionless factor given by,

$$\zeta = \frac{10\psi(1+\psi^3)}{-\psi^6 + 5\psi^2 - 9\psi + 5}, \tag{3.22}$$

where $\psi = R_d/\delta$ is the ratio between the radii of the dislocation bubble and the Wigner-Seitz cell.

The bubble volume is calculated via,

$$\frac{dV_d}{dt} = \frac{\Omega_{fg}}{N_d}\frac{\partial m_d}{\partial t} + \Omega\frac{\partial n_{iv}}{\partial t}, \tag{3.23}$$

where $\Omega_{fg} = 8.5 \cdot 10^{-29}$ m^3 is the van der Waals atomic volume for Xe.

The bubble radius is calculated from the bubble volume,

$$R_d = \sqrt[3]{\frac{3V_d}{4\pi}}. \tag{3.24}$$

The swelling due to dislocation bubbles is calculated as,

$$\left(\frac{\Delta V}{V}\right)_d = V_d N_d. \tag{3.25}$$

The formulation of vacancy arrival at the dislocation bubble should be re-investigated because it is unclear whether the vacancy would travel along the dislocation to the bubble or would incorporate into the dislocation line causing dislocation climb.

Additionally, the van der Waals atomic volume arriving with Xe atoms should be replaced with the appropriate volume of the defect that dominates Xe diffusion. If Xe interstitial diffusion is dominant, there should be no volume arriving with Xe to the bubble. If the Xe clustered with two vacancies dominates Xe diffusion, then the volume arriving should be 2Ω.

3.9 Bubble Coalescence

The dislocation bubbles may reach sufficiently large sizes that their radii are comparable to the inter-bubble distance. In such a senario, dislocation bubbles are allowed to coalescence, decreasing their number density, but maintaining the bubble gas content. The equation for the variation of the number density of dislocation bubbles as the size changes is based on the nearest-neighbor distribution of hard sphere [31] and is given by,

$$\frac{dN_d}{dV_d} = -4\lambda N_d^2. \tag{3.26}$$

where $\lambda = (2-\xi)/[2(1-\lambda)^3]$ is a correction factor for the hard sphere assumption, and $\xi = \frac{4}{3}\pi R_d^3 N_d$ is the porosity associated with dislocation bubbles.

3.10 PolyPole-1 and PolyPole-2 Algorithms

Sifgrs contains two models – PolyPole-1 [32] and PolyPole-2 [11] – to estimate the distribution of intra-granular fission gas, intra-granular bubbles, and ultimately the flux to the grain boundary. While similar in nature, there are key differences between the two algorithms that will be shown to be important for accurately capturing the behavior in uranium nitride.

The PolyPole algorithms solve for the amount of gas in the matrix c, the amount of gas in intragranular bubbles m, and release of fission gas from the grain to the grain boundaries. This intragranular fission gas release problem is condensed into two partial differential equations,

$$\begin{aligned} \frac{\partial c}{\partial t} &= D_{fg}\Delta^2 c - gc + bm + \dot{G}, \\ \frac{\partial m}{\partial t} &= gc - bm, \end{aligned} \tag{3.27}$$

where c [m^{-3}] is the concentration of single gas atoms dissolved in the lattice, m [m^{-3}] is the concentration of gas atoms in intra-granular bubbles, t [s] is the time, g [s^{-1}] is the trapping rate of gas atoms at bubbles, b [s^{-1}] is the rate of irradiation-induced gas atom resolution from bubbles back into the lattice, and G [$\mathrm{m}^{-3}\mathrm{s}^{-1}$] is the gas generation term. The first equation tracks the change in single gas atom concentration in the lattice subject to the effects of diffusion, trapping, resolution, and generation. The second equation tracks the change in the concentration of gas atoms in intra-granular bubbles subject to the effects of trapping and resolution.

To solve these PDEs, several assumptions are made. First, the grain is assumed to have a spherical geometry with grain radius a. The solutions $c(r,t)$ and $m(r,t)$ are assumed to take a modal form of the analytic solution to the spatial problem at constant conditions, where the time part of the solution is handled by using polynomials of dt with pole functions of the spatial solution as the coefficients.

If the rates of trapping and resolution are much higher than the rate of diffusion to the grain boundaries, known as the quasi-stationary approximation, the second equation in Eq. (3.27) can be written in the steady-state condition,

$$\frac{\partial m}{\partial t} = gc - bm = 0, \tag{3.28}$$

which provides the equilibrium ratio of the concentration of gas atoms in the lattice to the concentration of gas atoms in the bubbles is equal to the ratio of the resolution rate to the trapping trapping rate, or $c/m = b/g$. To help simplify Eq. (3.27), the effective diffusion coefficient can be defined that accounts for the reduced apparent diffusion due to gas being trapped in bubbles [11, 33], given by,

$$D_{eff} = \left(\frac{b}{b+g}\right) D. \tag{3.29}$$

A total gas concentration can be defined as $c_t = c + m$. Finally, with the quasi-stationary approximation resulting in Eq. (3.28) and the defined effective diffusion coefficient in Eq. (3.29), Eq. (3.27) can be reduced to,

$$\frac{\partial c_t}{\partial t} = D_{eff}\Delta^2 c_t + \dot{G}. \tag{3.30}$$

The quasi-stationary approximation states that the trapping and resolution rates are substantially greater than the rate by which gas diffuses to grain boundaries, or in other words, that a

gas atom experiences many interactions with bubbles before reaching the grain boundary. It is true if

$$b + g \gg D\pi^2/a^2. \tag{3.31}$$

However, this relation does not always hold. To help illustrate this point, assume high temperatures where resolution is substantially slower than migration, so we can ignore b and simplify the relation to $g = 4\pi DRN \gg D\pi^2/a^2$, which rearranges to $RNa^2 \gg \pi/4$. For a large number density of large bubbles in large grains, this relation may hold, but if the bubbles are small and infrequent, and grain size is relatively small, this relation will not hold. For example, allow for the realistic values for bubbles in UN of $R = 10^{-9}$ m, $N = 10^{19}$ m^{-3}, and $a = 10^{-5}$ m. $RNa^2 = 1$ which is not substantially greater than $\pi/4$. In high burnup UO_2, the bubble density is greater, $N = 10^{24}$ m^{-3}, allowing the approximation to hold assuming no quick transients.

PolyPole-1 makes the quasi-stationary approximation while *PolyPole-2* does not [11,32]. This makes *PolyPole-2* the suitable choice for high temperature transients where the quasi-stationary approximation does not hold. Both algorithms were originally written assuming only one population of bubbles with mean sizes, densities, and gas concentrations, and each has slightly different adaptations to include the second dislocation bubble population. Both adaptations should be revisited in the future to ensure correctness, as both attempt to apply the two different resolution rates to total gas concentrations in the bubbles m instead of their respective individual concentrations m_b and m_d.

PolyPole-1 adds the trapping to resolution ratios from dislocation bubbles to the effective diffusion coefficient,

$$D_{eff} = \left(\frac{1}{1 + \frac{g_b}{b_b} + \frac{g_d + g'}{b_d}} \right) D, \tag{3.32}$$

and calculates the amount of gas atoms that remain in bulk and dislocation bubbles as $g_b c/b_b$ and $(g_d + g')/b_d$, respectively.

PolyPole-2 is a complicated algorithm with single trapping and resolution rates as inputs. Therefore, to include the second population of dislocation bubbles, a crude adaptation was put in place where total trapping and resolution rates are sent to *PolyPole-2* as $g = g_b + g_d + g'$ and $b = b_b + b_d$. *PolyPole-2* then solves for the gas concentration in the matrix c and the total gas concentration in all bubbles m. Finally, the change in the concentration of gas atoms in each bubble type is fractioned out by the ratio given by,

$$\begin{aligned} \text{ratio} &= \tfrac{g_b c - b_b m_b}{(g_b + g_d + g')c - b_b m_b - b_d m_d} \\ \Delta m_b &= (\text{ratio})\Delta m \\ \Delta m_d &= (1 - \text{ratio})\Delta m \end{aligned} \tag{3.33}$$

The correct approach would attempt to solve the three PDEs instead of two:

$$\begin{aligned} \tfrac{\partial c}{\partial t} &= D_{fg}\Delta^2 c - (g_b + g_d + g')c + b_b m_b + b_d m_d + \dot{G}, \\ \tfrac{\partial m_b}{\partial t} &= g_b c - b_b m_b, \\ \tfrac{\partial m_d}{\partial t} &= (g_d + g')c - b_b m_d. \end{aligned} \tag{3.34}$$

In future work, the `PolyPole-2` algorithm should be re-derived using the second population of bubbles.

3.11 Dislocation Specific Parameters

With the introduction of dislocations into the Sifgrs models, there are a number of dislocation specific physics that are useful for understanding the evolution of the model over time. These will be described briefly here, and will be utilized in Section 3.12.

3.11.1 Dislocation Punching Threshold

If a bubble absorbs too many gas atoms and not enough vacancies, it is possible that the pressure of the fission gas inside the bubble exerts such a large stress on the surrounding lattice that dislocation loops form to add volume to the bubble and relieve the pressure. This process is called loop punching. The pressure threshold for loop punching is given by,

$$P_{dis} = \frac{Gb}{R_b} + P_{eq} \tag{3.35}$$

where $G = \frac{E}{2(1+\nu)}$ is the sheer modulus, b is the length of the Burger's vector, R_b is the bubble radius, and $P_{eq} = 2\gamma/R_b$ is the bubble equilibrium pressure. This threshold is helpful to visualize to ensure that the growth regime via the diffusive process is the relevant bubble growth physics.

3.11.2 Dislocation Coverage

As dislocation bubbles grow to sufficient sizes such that they may interconnect, the eventual release to the plenum needs to be tracked to accurately estimate fission gas release. Conversely, if the overall dislocation coverage by bubbles is low, the dislocation bubbles will likely remain isolated and not contribute to fission gas release. To this end, a dislocation coverage fraction can be estimated, similar to grain boundary coverage. However, grain boundaries are two dimensional while dislocation lines are one-dimensional, making it more difficult for dislocation bubbles to form interconnected pathways than grain-boundary bubbles.

Making the assumption that the spherical dislocation bubbles are positioned with their centers located directly on dislocation lines, the dislocation coverage is calculated by,

$$\mathrm{DC}[\%] = 100\% \times \frac{2R_d N_d}{\rho_d}. \tag{3.36}$$

3.11.3 Empirical Dislocation Density Function

The last piece required for the dislocation bubble evolution model is an estimation of the dislocation line density as a function of burnup and time. In lieu of a mechanistic model (see Section 4.2), an analytical empirical description of the dislocation density as a function of burnup and temperature was created as a temporary placeholder to provide some insights into how a variable dislocation density should behave in the overall fission gas model.

Table 3.2: Empirical Linear Dislocation Density Equation Parameters (Eq. (3.37))

Parameter	Value	Units
ρ_0	10^{13}	m^{-2}
C_1	$1.589 \cdot 10^{16}$	m^{-2} (FIMA)$^{-1}$
F_0	$1.589 \cdot 10^{16}$	m^{-2} (FIMA)$^{-1}$
C_2	58.18	m^{-2} K^{-1}
T_0	906.3[a]	K

[a] 1108.0 K for UN

Ray and Blank [6] performed a transmission electron microscopy (TEM) analysis of the defects in mixed carbide fuel, $U_{0.8}Pu_{0.2}C$, with burnups up to 11% FIMA. They found that the density of small intragranular bubbles depends strongly on the dislocation density. Ray and Blank [6] noted that the dislocation density appears to follow a simple linear relation with burnup at a constant temperature. The dislocation density data also appears to follow a linear relationship with temperature at a constant burnup:

$$\rho_d = \begin{cases} \rho_0 & \text{if } C_1(F-F_0)+C_2(T-T_0) \leq \rho_0 \\ C_1(F-F_0)+C_2(T-T_0) & \text{if } C_1(F-F_0)+C_2(T-T_0) > \rho_0 \end{cases} \tag{3.37}$$

where ρ_0 is the minimum dislocation density observed, existing from fabrication. The parameter values for this equation are given in Table 3.2.

During testing, the linear dependence with burnup resulted in poor comparison to experimental measurements of fission gas swelling [14]. A second formulation developed for high-burnup UO_2 was tested, which shows more of an exponential increase as a function of burnup [34]:

$$\rho_d = \rho_0 \exp\left(\frac{cF}{\max(T_d, T_0 - T)}\right). \tag{3.38}$$

The condition that the temperature difference in the denominator never be less than a minimum T_d prevents the asymptotic behavior as the temperature approaches T_0. Another condition applied is that the overall dislocation density not exceed a value of $10^{15} m^{-2}$, which would be associated physically with the saturation of the dislocation network. The results of fitting this exponential function to the dislocation density data from carbide fuel are shown in Figs. 3.13 and 3.14, with values given in Table 3.3. The value of ρ_0 for UO_2 is $6 \cdot 10^{13}$ m^{-2}. Although this formulation does not fit the limited UC data as well as the simple linear function (Eq. (3.37)), it is adopted for this work because it produces better swelling results.

3.12 Results

A rough calibration of the many input parameters in Sifgrs was performed, with an emphasis on the intragranular fission gas swelling results, shown in Fig. 3.15. Table 3.4 lists the inputs for UN, their sources, and the calibration applied to them. This list compliments the diffusivity

Table 3.3: Empirical Exponential Dislocation Density Equation Parameters (Eq. (3.38))

Parameter	Value for UC data [6]	Value used for UN	Units
ρ_0	$2 \cdot 10^{13}$	10^{12}	m^{-2}
c	38806	49000	K $(FIMA)^{-1}$
T_0	2000.6	1900.0	K
T_d	-	150.0	K

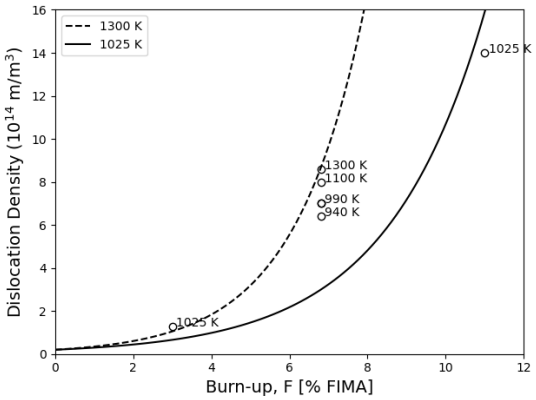

Figure 3.13: Dislocation density in UC as a function of burnup using the exponential equation in Eq. (3.38) with parameters in Table 3.3. The data is from [6].

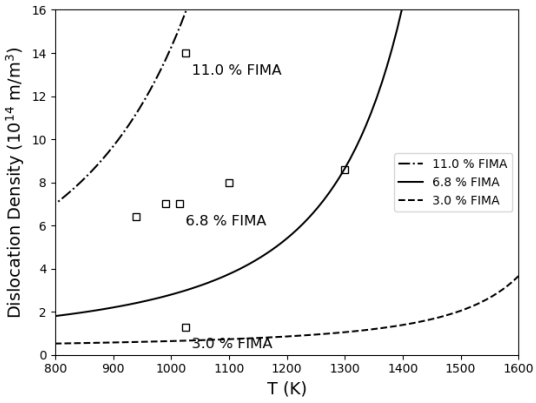

Figure 3.14: Dislocation density in UC as a function of temperature at three different burnup values using the exponential equation in Eq. (3.38) with parameters in Table 3.3. The data is from [6].

function parameters in Table 3.1 and the dislocation density function parameters given in Table 3.3. The calibrated values are within an order of magnitude of the initial values, and are certainly within the uncertainty range for those values. The placeholder empirical dislocation density function has the strongest effect and underwent the largest changes. It was beneficial to lower the overall dislocation density (ρ_0), and increase the dependence on burnup and temperature (c). In addition to lowering the overall dislocation density, the dislocation bubble nucleation factor was lowered by half of the starting value based on previous modeling work [4] and the value found for UC in Section 3.5. The bulk diffusion coefficients were increased by a factor of 5, while the enhanced diffusion coefficients of fission gas and vacancies near dislocations (Sections 3.7 and 3.8) are only $10\times$ those in the bulk, affecting gas atom trapping and the size growth of dislocation bubbles. However, trapping of gas atoms at dislocation lines was increased by a factor of 3. These values will certainly be revisited as the diffusivity and dislocation density calculations are further improved by LLS calculations and mechanistic model development underway, described in Section 4.2.

The Sifgrs calculation results signify that the breakaway swelling behavior is directly related to the balance of gas in the two intragranular bubble populations. The bulk intragranular bubble volumes and dislocation bubble volumes sum to give a total calculated intragranular swelling, shown by the solid blue line in Fig. 3.15. At low temperatures, the bulk bubble swelling, shown in green, is dominant and is nearly constant as temperature increases. At these lower temperatures, below $\sim$1200 K, athermal (D_3) diffusion of Xe is dominant. A slight slope still occurs due to the increased swelling from dislocation bubbles, due to the increasing dislocation density, shown in Fig. 3.16. Above $\sim$1200 K, irradiation-enhanced (D_2) diffusion of Xe exceeds athermal (D_3) diffusion, which causes the trapping at dislocations and the trapping at and swelling of dislocation bubbles to increase with temperature. As the temperature increases further into the breakaway swelling region, the swelling due to dislocation bubbles quickly increases, as more gas is trapped at dislocations than in the bulk intragranular bubbles due to the increasing dislocation density. The swelling due to dislocation bubbles is additionally boosted around 1700-1800 K due to the transition to thermal-equilibrium (D_1) of both vacancies and Xe atoms.

Fig. 3.17 shows the fraction of the dislocation line length covered by bubbles. This fraction tends to increase with temperature over a large temperature range and decreases slightly with increasing burnup. The temperature dependence relies on multiple factors including Xe diffusion, vacancy diffusion, and dislocation density, and roughly resembles the shape of the bubble radius plot (Fig. 3.19). The sharp increase and decrease between 1200 and 1800 K, or in other words the 'bump' in the plot, corresponds to the 'bump' in the irradiation-enhanced diffusion of Xe interstitials shown in Fig. 3.7. As burnup increases, the average dislocation bubble size increases slightly in the simulation, but the average number density of bubbles along a given dislocation line decreases due to some amount of coalescence and destruction by resolution, giving a slight overall decrease in fractional coverage.

Inter-granular swelling is dependent on gas atoms reaching the grain boundaries, and is therefore affected by many factors including changes in diffusivity and impediments to gas atom migration caused by trapping at dislocations and intragranular bubbles. The swelling due to intergranular bubbles is shown by the dashed orange lines in Fig. 3.15 for reference, but is not comparable to the intragranular swelling measurements shown in the figure.

Table 3.4: List of Sifgrs model parameters used for UN. The starting values are shown for reference, with the calibration multipliers determined from comparison to the DN1 and DN2 mixed nitride experiment [14] also given. Acronyms used are density functional theory (DFT), empirical potentials (EP), lower length-scale (LLS), molecular dynamics (MD).

Parameter	Starting Value	Source	Calibration
$D_1^{V_U}$	Table 3.1	LLS - DFT and EP	$\times 5$
$D_2^{V_U}$	Table 3.1	LLS - Centipede	$\times 5$
D_1^{Xe}	Table 3.1	LLS - DFT and EP	$\times 5$
D_2^{Xe}	Table 3.1	LLS - Centipede	$\times 5$
D_3^{Xe}	Table 3.1	LLS - MD	$\times 5$
Ω_{fg}	$8.5{\cdot}10^{-29}$ m^3	[35]	-
f_n	$1{\cdot}10^{-6}$	inherited from U_3Si_2 [18, 22, 26]	-
b_0	Eq. (3.16)	LLS - Binary collision approximation [28]	-
f_{tr}	1	inherited from U_3Si_2	-
a	$4.889{\cdot}10^{-10}$ m	[9]	-
Ω	$a^3/4$		-
γ	1.74 Jm^{-2}	LLS - DFT [29, 30]	-
D_{gb}^v	$10^6 D^{V_U}$	[9]	-
δ_{gb}	$4{\cdot}10^{-10}$ m	assumption in [36] for UC	-
$N_{gf,0}$	$2{\cdot}10^{13}$ m^{-2}	assumption	-
θ	73°	inherited from LLS simulations of U_3Si_2 [22]	-
R_{gf}	$2.42{\cdot}10^{-10}$ m	based on θ	-
r_{gr}	$6{\cdot}10^{-6}$ m	approximate constant value [9, 37]	-
$F_{c,sat}$	0.5	based on UO_2 [38]	-
D_d^v	$10^2 D^{V_U}$	assumed	$\times 0.1$
D_d^{Xe}	$10^2 D^{Xe}$	assumed	$\times 0.1$
K	$1{\cdot}10^{-6}$ bubble m^{-1}	based on data in UC [6]	$\times 0.5$
r_d	$5b = 5a/\sqrt{2}$	[4]	-
$f_{\text{tr,disl}}$	1	assumed	$\times 3$
ρ_d	Table 3.3	based on data in UC [6]	Table 3.3

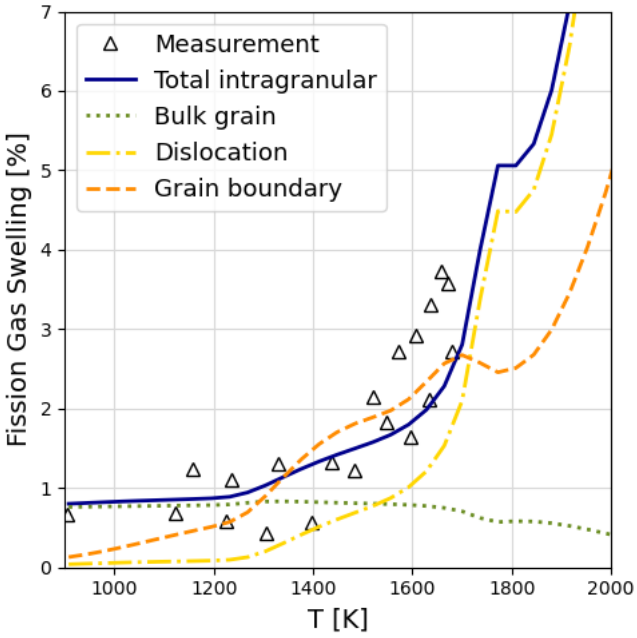

(a) 1.1% FIMA

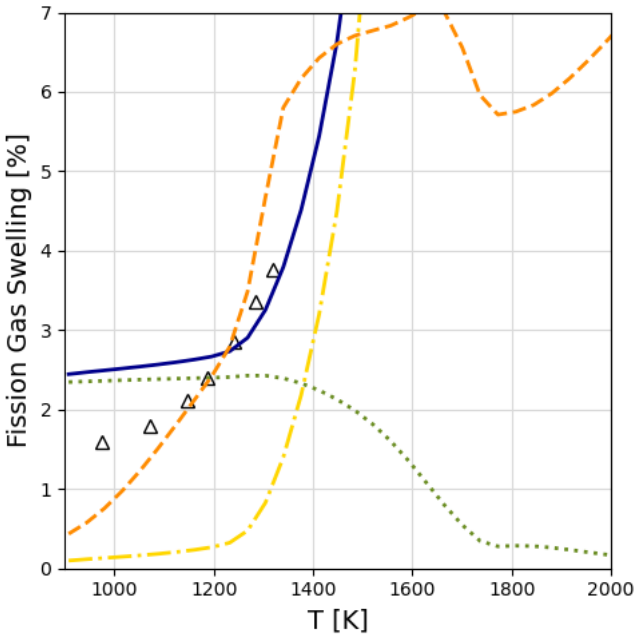

(b) 3.2% FIMA

Figure 3.15: Fission gas bubble swelling at (a) 1.1% FIMA and (b) 3.2% FIMA compared to intragranular bubble swelling measurements [14]. Bulk and dislocation bubbles contribute to intragranular swelling. The swelling due to intergranular bubbles is shown in orange as well for information, but is not comparable to the measurements.

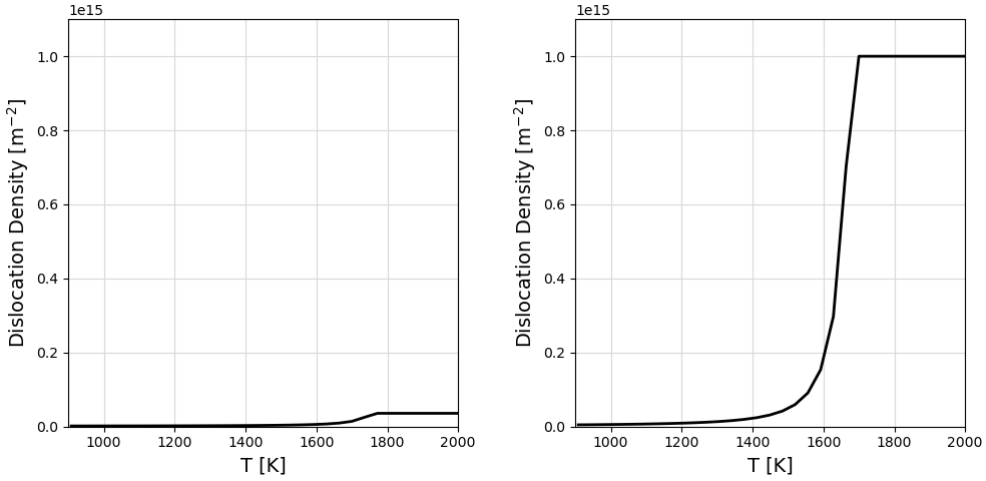

(a) 1.1% FIMA (b) 3.2% FIMA

Figure 3.16: Calculated dislocation density at (a) 1.1% FIMA and (b) 3.2% FIMA.

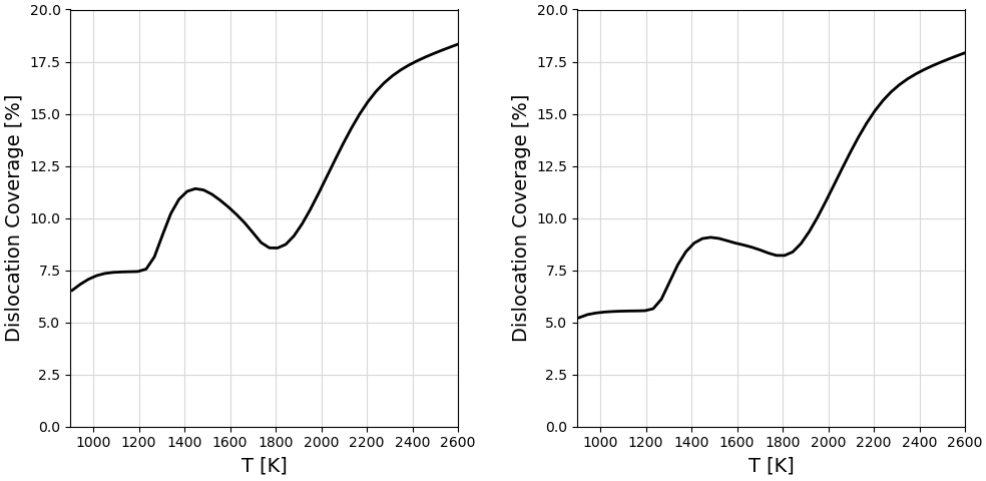

(a) 1.1% FIMA (b) 3.2% FIMA

Figure 3.17: Calculated dislocation coverage at (a) 1.1% FIMA and (b) 3.2% FIMA.

The Sifgrs calculations match the experimental measurements of intragranular bubble swelling shown in Figs. 3.15 and 3.18, and intragranular bubble size shown in Fig. 3.19 very well. At higher burnup values, the low-temperature intragranular swelling appears to be overpredicted; however, this difference is likely due to how the bubbles were measured. The replica-electron-microscopy method has limited resolution and cannot reliably observe bubbles with radii less than roughly 10 nm. Based on the bubble radii shown in Fig. 3.19, and size of the average bulk intragranular bubble is below the resolution threshold. So the swelling at higher burnup and lower temperatures is likely underestimated. Similarly, only the average dislocation bubble size, shown by the yellow line in Fig. 3.19 may be directly comparable to the measured average bubble size shown.

If the bubble pressure exceeds the dislocation loop punching threshold pressure, the bubbles may increase their size by loop punching, which would also cause some amount of increase in the dislocation density. Fig. 3.20 shows the calculated bubble pressures, equilibrium pressures, and loop punching threshold pressures for the three types of bubbles at 3.2% FIMA. None of the bubbles are calculated to exceed the dislocation punching threshold above 900 K, although they may exceed the threshold at much lower temperatures near the periphery of the fuel pellet. The bulk bubbles are always at the equilibrium pressure due to plentiful arrival of vacancies. The dislocation bubbles exceed their equilibrium pressures as temperature increases due to relatively more efficient trapping leading to absorption at bubbles of gas atoms than vacancies at dislocations. The grain boundary bubbles exceed their equilibrium pressures until temperatures are above $\sim$1600 K, where thermal equilibrium (D_1) vacancy diffusion dominates and quickly increases with temperature, allowing sufficient vacancies to migrate to grain boundary bubbles and relieve the pressure.

Fig. 3.21 shows where the gas that is generated is located, including fission gas release (FGR), as a function of temperature. Little gas remains in the matrix, especially at temperatures greater than 1200 K, when Xe diffusion increases by irradiation-enhanced diffusion of Xe interstitials. At low temperatures the majority of the gas is trapped in the bulk bubbles, and at higher temperatures the majority of the gas is trapped in the dislocation bubbles. The trapping of gas in the intragranular bubbles slows the gas migration to the grain boundaries, and ultimately impedes gas from being released. The shape of the FGR at 3.2% FIMA as a function of temperature, like the dislocation coverage and average dislocation bubble radius, shows a sharp increase, a relative maximum, and a sharp decrease between 1200 and 1800 K that corresponds to the 'bump' in the irradiation-enhanced diffusion of Xe interstitials shown in Fig. 3.7.

3.13 Assessments Using New Model

3.13.1 SP1

The SP-1 irradiation test was described in a previous milestone report [10], and is revisited using the new model. Four UN pins were irradiated in EBR-II in the SP-100 space reactor test assembly, and two pins, NBU-2 and NBU-3, were examined post-irradiation. The burnup was relatively low at 0.81% FIMA. The temperature of the fuel was very high, with NBU-3 centerline and fuel surface temperatures estimated as 1950 and 1860 K, respectively.

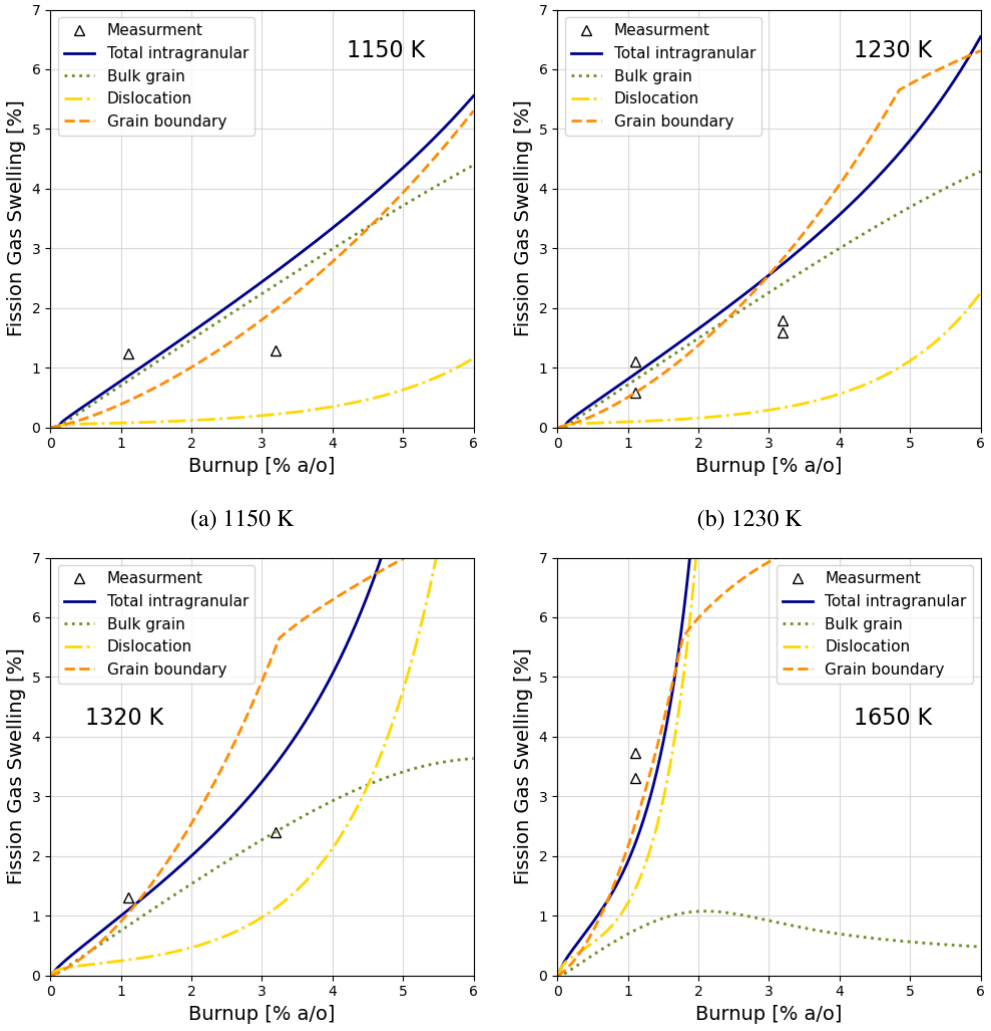

(a) 1150 K

(b) 1230 K

(c) 1320 K

(d) 1650 K

Figure 3.18: Fission gas bubble swelling at (a) 1150 K, (b) 1230 K, (c) 1320 K and (d) 1650 K compared to intragranular bubble swelling measurements [14]. Bulk and dislocation bubbles contribute to intragranular swelling. The swelling due to intergranular bubbles is shown in orange for information, but is not comparable to the measurements.

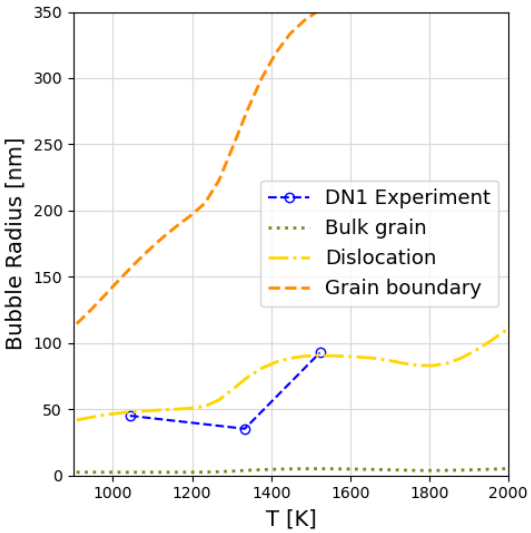

Figure 3.19: Average bubble radii compared to the average measured intragranular bubble radii [14].

The NBU-3 pin was measured to have significant FGR at 15%. However, the amount of FGR in the BISON simulation was trivially small, 0.001%. The calculated fuel centerline temperature reached 1939 K, and the fuel surface temperature reached 1644 K, which are somewhat lower values than what was estimated for the experiment.

The NBU-3 pin had a radial swelling of 3.7% and an axial swelling of 1.2%, resulting in a volumetric swelling of 8.8%. The Sifgrs model is unable to capture bulk macroscopic swelling anisotropy due to axial stress from contact with the cladding. The calculated isotropic swelling was 5.6%, which is 36% lower than the measured value.

3.13.2 JOYO

Two He-bonded (U,Pu)N fuel pins were irradiated in the experimental fast reactor JOYO [39] to a burnup of 4.3% FIMA. The linear heating rate was 75 kW/m. The cladding was 15Cr-20Ni stainless steel. The difference between the two pins are the He-gap widths given in Table 3.5. The measured swelling and fission gas release (FGR) values are given in Table 3.6. These results compare fairly well. The calculated swelling results are within 0.6%-swelling of the measured values, and the calculated FGR results are within 2%-FGR of the measured values.

3.14 Discussion and Future Work

The results presented provide a promising explanation of why there is an abrupt increase in intragranular swelling at a transition temperature. The answer provided is a transition from bulk bubble swelling at low temperature to dislocation bubble swelling at higher temperatures. While this explanation is encouraging, it is one of many possible explanations and has some amount of uncertainty associated with it. Much of this uncertainty is related to the temperature dependence

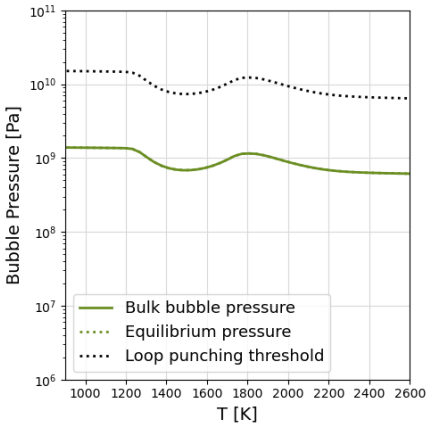

(a) Bulk

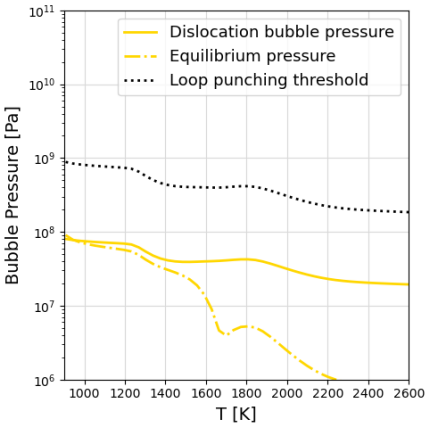

(b) Dislocation

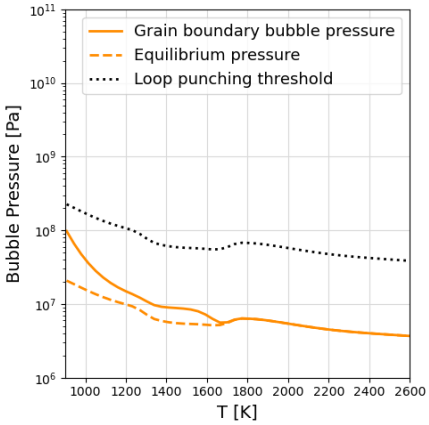

(c) Grain boundary

Figure 3.20: Calculated bubble pressures, equilibrium pressure, and dislocation punching threshold at 3.2% FIMA for (a) bulk, (b) dislocation, and (c) grain boundary types of bubbles.

Table 3.5: JOYO test specifications [39].

Pin:	L413	L414	units
Cladding OD	8.50	8.50	mm
Cladding ID	7.60	7.60	mm
Cladding thickness	0.45	0.45	mm
Pellet OD	7.28	7.43	mm
Diametral gap	0.32	0.17	mm
Stack height	200.1	200.1	mm
Pellet height	8	8	mm
Pellet density (before irradiation)	84.8	86.0	% TD

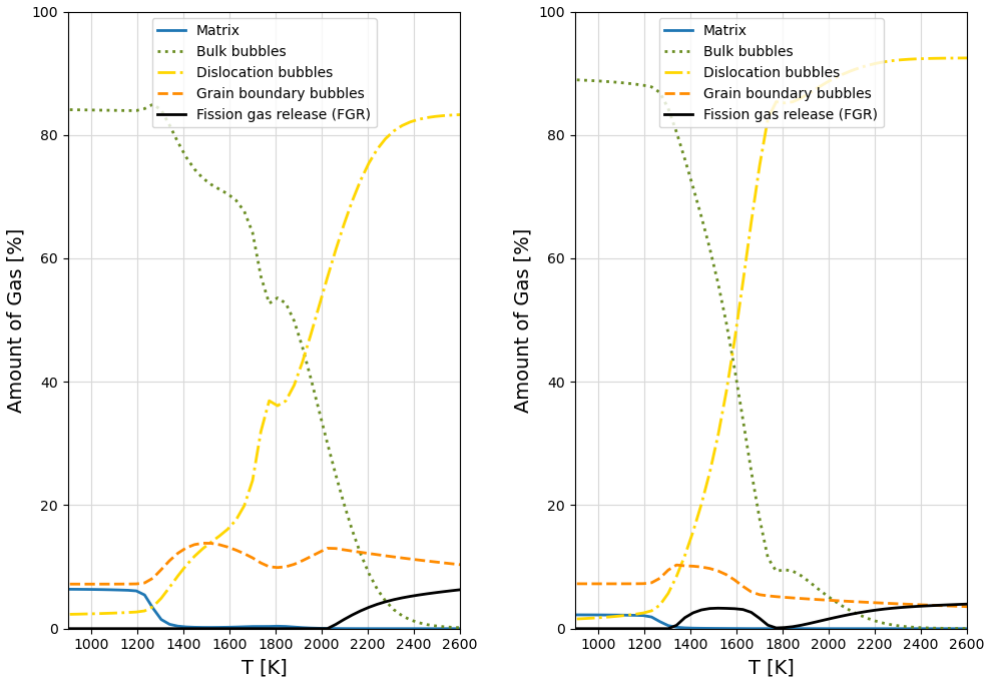

(a) 1.1% FIMA

(b) 3.2% FIMA

Figure 3.21: Calculated fraction of gas generated in the matrix, bulk bubbles, dislocation bubbles, intergranular bubbles, and released at (a) 1.1% FIMA and (b) 3.2% FIMA.

Table 3.6: JOYO pin measurements of swelling and fission gas release compared to the calculated results.

Pin:	L413		L414	
	Experiment	Calculated	Experiment	Calculated
Swelling (%)	7.4	6.8	6.7	6.4
FGR (%)	3.3	5.2	5.2	4.5

of the dislocation density, which is based on very limited experimental data. This highlights the importance of a mechanistic dislocation model, discussed in the next chapter.

While the JOYO assessment calculation gives reasonable results, the low burnup and high temperature SP1 assessment significantly underestimates FGR. This is due to the dislocation bubbles trapping gas inside the grain and preventing it from reaching the grain boundaries at high temperatures. This supports the idea that the dislocation density should decrease at these very high temperatures, which should be captured in a mechanistic model. A decrease in dislocation density at high temperatures would allow more gas to escape the grain and decrease the microscopic intragranular swelling, which would allow the turn-over seen in Fig. 3.2 that occurs in carbide fuel at high temperatures associated with increased grain boundary bubble size.

The swelling data and assessment data were produced using mixed nitride fuel with 20% Pu, $(U_{0.8},Pu_{0.2})N$, while the calculations presented are strictly UN. It is assumed here that neglecting the fraction of Pu included in the fuel has a smaller impact than many of the larger uncertainties associated with this modeling work.

An 'average' N_2 partial pressure was assumed, but the diffusivity values of the various defects can change by several orders of magnitude simply by moving towards the U-rich and N-rich boundaries in Fig. 3.6 [23]. The fuel was fabricated under high N_2 partial pressure of 0.92 atm [40]. This sensitivity is handled in Centipede and should be incorporated in the fission gas modeling. Additionally, the dominant diffusion mechanism, e.g. interstitial or vacancy cluster, changes due to chemistry changes. Similarly, carbon and oxygen impurities can cause significant changes in the diffusivity values and the dominant diffusion mechanism, and should be investigated.

Some assumptions were made to enable the `PolyPole-2` algorithm to handle two bubble populations. The impact these assumptions have on the accuracy of the calculation should be investigated, and a potential rewrite of the algorithm to handle multiple bubble populations should be explored. Additionally, the validity range and impact of the quasi-stationary approximation for UN should be clearly documented.

The bubble radial growth model has some assumptions that should be revisited inspired by updates to Sifgrs in a previous milestone [41]. The volume that arrives with Xe should be updated to consider the defect type dominating its diffusion. The arrival of vacancies at the dislocations should be re-visited, as it is not clear whether vacancies would diffuse to the bubbles or incorporate in the dislocation line causing it to climb. The possibility of over-pressurization to the point of dislocation loop punching was considered, but the opposite situation of void swelling was not. If vacancy arrival is greater than Xe arrival to grain boundaries at high temperature, the grain boundary bubbles could be in a void swelling regime that increases both fission gas release and overall swelling. To investigate this possibility, the revised reaction rate for vacancies with grain boundary bubbles reported in [41] should be utilized.

4 Dislocation Density Modeling

Dislocations have been modeled in variety of ways, both in discrete, spatially resolved simulations [42–44], as well as more simple rate-theory cluster dynamics type models [45–48]. Due to the availability of lower-length scale data and the successes with cluster dynamics in mechanistically capturing diffusive processes, a dislocation growth model was built in Centipede to eventually replace the empirical model utilized now for the BISON UN fission gas swelling and release model. This model required a number of advancements in both Centipede and the atomistic data. In particular, the inclusion of larger interstitial clusters may have a large impact on dislocation growth. The following sections outline these improvements, ultimately leading to a comparison of computed and measured dislocation line densities.

4.1 Atomistic calculations

Mechanistic models have repeatedly demonstrated their ability to describe large-scale thermomechanical behaviors observed experimentally. Yet, the uncertainty of these predictions will only be as low as that of the calibration data. As such, the approach presented in this work can greatly benefit from the use of ab-initio calculations to accurately determine the energetics of key interstitial clusters, and provide valuable inputs to parameterize the dislocations nucleation and growth.

4.1.1 Computational details

First-principles calculations were performed using Density Functional Theory (DFT) with the projector augmented wave (PAW) method [49, 50] as implemented in the VASP (Vienna Ab-initio Simulation Package) code [51–53]. The results were obtained using the generalized gradient approximation (GGA) for the exchange-correlation functional in the Perdew-Burke-Ernzerhof (PBE) form [54]. Following the conclusions of Kocevski *et al.* [55], no Hubbard correction was used, and spin-orbit coupling was neglected. Using this approach, the ground-state of UN is cubic and ferromagnetic. The plane wave basis cutoff was set to 400 eV. Supercells of 216 atoms ($3 \times 3 \times 3$ unit cells) were used in order to accommodate the largest clusters (up to 10 defects). All the calculations were performed at constant pressure, the residual stresses of all systems were checked to remain lower than 1 kBar. $2 \times 2 \times 2$ k-point grids were used in these calculations, achieving a k-sampling equivalent to a unit cell with a 6x6x6 grid. The Fermi-Dirac broadening scheme was used with a 0.2 eV smearing.

We note that the accuracy expected from such a calculation setup is voluntarily limited. This work involves the screening of dozens of cluster configurations, among which only a few will be thermodynamically relevant. Our strategy is to firstly screen the phase space with a frugal setup,

and then to increase the accuracy for the few interesting configurations. This compromise allows to spare computational resources while obtaining a satisfactory accuracy on the key values that rule the thermodynamics and the kinetics of the system.

The binding enthalpies reported in this section are expressed as follows:

$$H^B = H^{tot}_{cluster} - \sum_{k=1}^{N} H^{tot}_k + (N-1)H^{tot}_{perfect} \tag{4.1}$$

where $H^{tot}_{cluster}$ is the total enthalpy of the system containing a N-defect cluster, H^{tot}_k are the respective enthalpies of the systems containing single defects constituting the cluster (the variable k designates each constituent), and $H^{tot}_{perfect}$ is the enthalpy of the defect-free system. Using this convention, negative binding enthalpies correspond to an attractive interaction.

4.1.2 Interstitial clusters in UN

First, we have verified that the ground-states of U_i and N_i single interstitial defects are respectively a $\{111\}$ dumbbell and a tetrahedral interstitial, in agreement with the available literature [56,57]. These configurations are used as references for the determination of cluster binding enthalpies in the following.

For each cluster size and composition, calculations have been performed with various initial configurations in order to explore as many as possible. Figure 4.1 displays the binding energy of the few stable configurations found for the $2U_i$-$2N_i$ cluster. As can be observed by comparing configurations D and G, almost similar cluster configurations (varying only by a slight shift of the N_i position) can lead to drastic differences in terms of enthalpy. Hence the importance of carefully screening possible configurations. Note that some cluster configurations exhibit a positive binding energy and are not shown here, as the interest is very limited.

For all cluster sizes up to $5U_i$-$5N_i$, the ground-state configurations are essentially composed of U dumbbells and N tetrahedral interstitials. The only exception being for U_i-N_i whose lowest energy state consists of a U_N antisite surrounded by two tetrahedral N_i interstitials in the $\{111\}$ direction (See Figure 4.2).

When compiling the lowest energy state found for each cluster size, it appears as a clear trend that the lowest energy growth path of such clusters is the addition of U_i and N_i defects, alternatively, in the $\{110\}$ direction (see Figure 4.2).

As shown in Figure 4.2, the binding enthalpy and the binding enthalpy per defect decrease (i.e. become more attractive) when increasing the cluster size. We note that non-stoichiometric clusters (e.g. $3U_i$-$2N_i$) follow this trend as well. Therefore, the growth of such clusters by capture of (radiation induced) fast-diffusing single interstitial defects is expected.

Interestingly, the lowest energy configurations of these clusters, shown in Figure 4.2, appear quite similar to the cross-section view of a $\langle 100 \rangle$ dislocation loop in UN (see Figure 4.3), which is expected to be the dominant loop according to experiments [58].

Even though the favorable $\{110\}$ orientation of such interstitial clusters is promising to model the dislocations nucleation and growth, our current DFT results are limited to longitudinal clusters, and not actual dislocation loops. Further calculations are currently being carried in order to

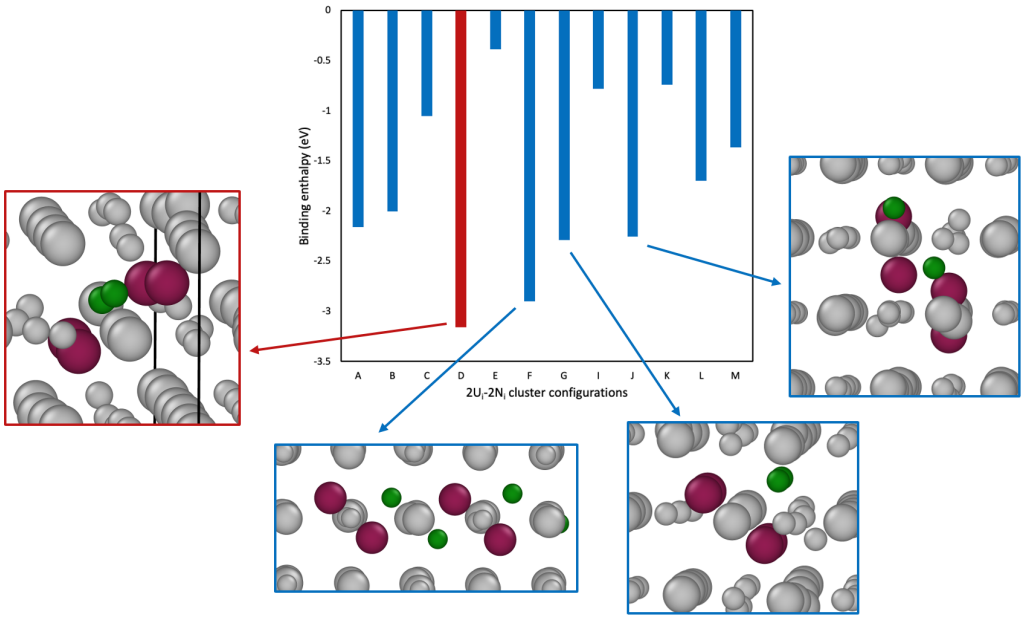

Figure 4.1: Binding enthalpy of various stable $2U_i$-$2N_i$ interstitial clusters. The configuration of the four most favorable clusters are shown to illustrate the variety of possible configurations.

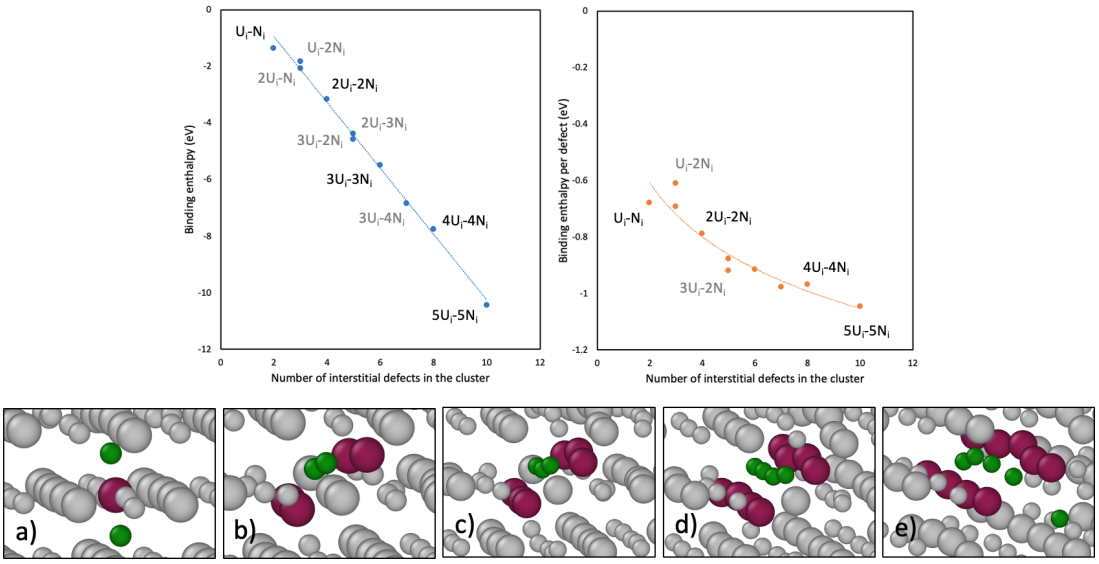

Figure 4.2: Binding enthalpy and binding enthalpy per defect of the lowest-energy cluster configurations for each size. Grayed labels indicate non-soichiometric clusters. The configurations of stoichiometric clusters from U_i-N_i to $5U_i$-$5N_i$ are shown.

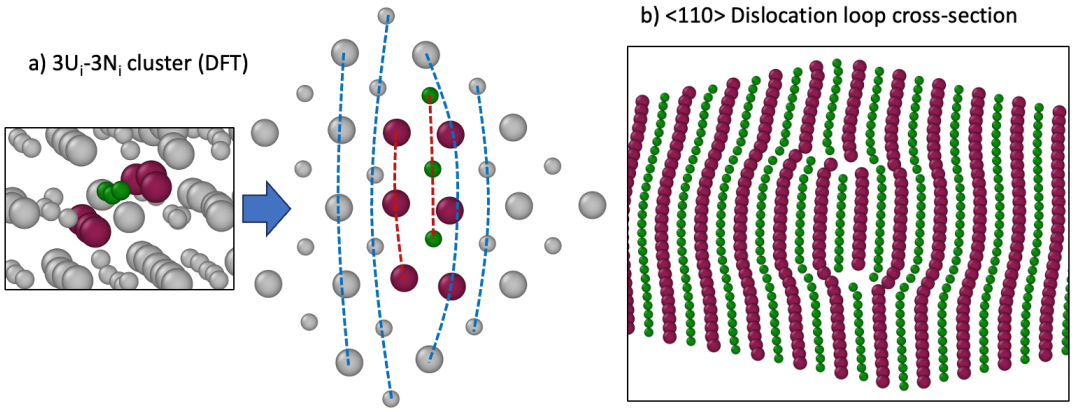

Figure 4.3: Illustration of the similarities between the lowest-energy interstitial clusters obtained from DFT and the structure of a $\langle 100 \rangle$ dislocation loop in UN.

determine how favorable is the growth of such clusters in the (orthogonal) $\{100\}$ direction. Indeed, the combined growth in both directions would lead the the formation of a double interstitial $\langle 100 \rangle$ plane, equivalent to a dislocation loop.

4.1.3 Dislocation line energy

Even though the interstitial clusters studied in this section are not exactly equivalent to a dislocation loop yet, it is interesting to compare the excess enthalpy of these clusters to the actual line energy of a dislocation in UN. Note that both quantities are not expected to be equal but the excess enthalpy should converge towards the line energy once the dislocation loop is fully formed.

For stoichiometric interstitial cluster, the excess enthalpies are expressed as follows:

$$H^{excess}_{jU_i - jN_i} = H^{tot}_{cluster} - \frac{N_{at} + 2j}{N_{at}} H^{tot}_{perfect} \tag{4.2}$$

where $H^{tot}_{cluster}$ is the total enthalpy of the system containing a $2j$-defect cluster, N_{at} is the number of atoms in the defect-free system (in the present case, 216), and $H^{tot}_{perfect}$ is the enthalpy of the defect-free system. Note that this expression can be generalized to non-stoichiometric clusters with the additional complexity of dealing with chemical potentials. The data presented in Figure 4.4 is limited to the stoichiometric clusters, considering that the binding enthalpy of stoichiometric and non-stoichiometric clusters seem to follow identical trends (see Figure 4.2).

The excess energy as a function of the cluster size is presented in Figure 4.4. As can be observed, there is a linear relation between the two, with a 3.73 eV/defect slope. Considering the length of the cluster as the distance between the two most extreme interstitial defects, the excess energy can be expressed as a function of the length and equals to 2.57 eV/Å.

From the Materials Science course of Prof. D. Trinkle [59] (available on the website of University of Illinois at Urbana-Champaign), the line energy of an edge dislocation can be ap-

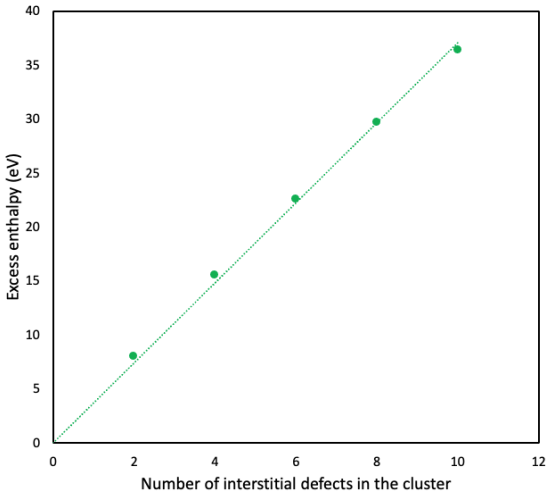

Figure 4.4: Interstitial clusters excess enthalpy as a function of the number of defects composing the cluster.

proximated as:

$$E^{line} = E^{core} + E^{elast} = \frac{G \cdot b^2}{2\pi} + \frac{G \cdot b^2}{4\pi(1-\nu)} \cdot \ln \frac{R}{r} \tag{4.3}$$

where ν is the Poisson ratio of the material, G is its shear modulus, and b is the Burgers vector of the dislocation. r is the core radius of the dislocation (usually assimilated as b) and R is the external radius of the elastic cylinder containing the dislocation. The value of R is not straight-forward at all, as it should in principle correspond to the crystal size, or the grain size in a practical example. In the present case, we can use R as a variable (as usually done in the literature [60]) to have a better idea of the line energy order of magnitude from elastic theory.

Considering $G = 1.05 \times 10^5$ MPa and $\nu = 0.27$ from the experimental literature [61], we obtain the curve shown in Figure 4.5, presented along with the dislocation line energy obtained by Parfitt *et al.* for a $\langle 100 \rangle$ dislocation in UO_2 [60]. The first observation is that the approximated line energy obtained in this work has the same order of magnitude as the results from Parfitt *et al.* in UO_2, which is comforting. The second observation is that the excess energy obtained from DFT is also of the same order (2.57 eV/Å). These two quantities are not equivalent and are not expected to match as what is modeled through DFT is not a dislocation loop but only a longitudinal interstitial cluster. However, we expect the values to be close once the cluster has grown enough in both $\{110\}$ and $\{100\}$ directions to form an interstitial plane that is equivalent to a $\langle 100 \rangle$ dislocation loop.

4.2 Cluster dynamics simulations

Dislocations in Centipede were incorporated very similar to other clusters, and follow the same guidelines of Free Energy Cluster Dynamics (FECD) that is the underlying foundation of all

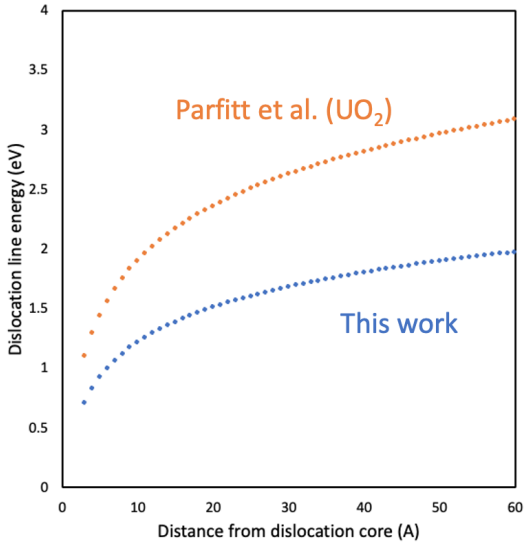

Figure 4.5: Dislocation line energy for a $\langle 110 \rangle$ edge dislocation in (orange) UO_2 reproduced from the plots presented in Ref. 60 and (blue) UN.

Centipede simulations [16]. In FECD, the rate for a particular reaction is defined by the change in the total Gibbs free energy of the system for the given reaction, along with a reaction coefficient that depends on geometric factors (sphere or cylindrical attraction laws), mobilities of the defects, and concentrations of the defects. By building up from fundamental calculations of defect energies, Centipede has been successful in qualitatively estimating self- and fission-gas diffusivities in UO_2 [17], doped UO_2 [18], TRISO [19], and uranium nitride [23].

The concentrations of defects in the UN fuel under irradiation are calculated by solving a set of ordinary differential equations (ODEs) that capture a number of phenomena including: production of Frenkel pairs through irradiation, mutual recombination of Frenkel pairs, interaction with sinks, clustering of point defects and dislocations. This latter defect is new, and will be discussed in detail. In addition, in order to capture the growth of dislocation loops, Centipede has recently been modified to allow for transient simulations instead of the typical steady-state solves. For completeness, a brief overview of the FECD math is repeated here.

4.2.1 Dislocations in Centipede

For the concentration, c_d, of a given defect, d, the ODE can be expressed as:

$$\frac{dc_d}{dt} = \dot{\beta}_d + \sum_C \dot{R}_{d,C}(c_d, c_C, T, G) - \sum_s \dot{S}_{d,s}(c_d, c_s, T, G) \tag{4.4}$$

where $\dot{\beta}_d$ describes the source rate of defects through irradiation. $\dot{R}_{d,C}$ and $\dot{S}_{d,s}$ are the cluster and sink rates, which depend on the defect concentration (c_d), the concentration of a given cluster (c_C), the sink concentration (c_s), the temperature T, and the free energy of the system

G. For Eq. (4.4), s represents the set of all sinks, which include bubbles, grain boundaries, and dislocations or other similar large defects.

The reaction rate, $\dot{R}_d$, for a given reaction, $A+B \rightarrow Y+Z$, can be expressed as:

$$\dot{R}_d = \begin{cases} \frac{k_i^2}{\Omega} D x_A x_B \left[1 - \exp\left(\frac{f}{k_B T}\right)\right], & \text{if } \Delta G_0 < 0, \\ \frac{k_i^2}{\Omega} D x_Y x_Z \left[\exp\left(\frac{-f}{k_B T}\right) - 1\right], & \text{otherwise} \end{cases} \tag{4.5}$$

where k_B is the Boltzmann constant, Ω is the atomic volume, k_i is a reaction rate constant, $D = D_A + D_B$ is the sum of the diffusivities of the reactants, and ΔG_0 is the change in energy due to the reaction. x_A and x_B are the atom fractions of the reactants and x_Y and x_Z are the atom fractions of the products. If the driving force, ΔG_0, is less than zero, the net rate is for the reaction to go forwards, otherwise it goes backwards. The driving force is given by the change in the free energy of the system due to the reaction:

$$f = \sum_p^P \frac{\partial G}{\partial x_p} - \sum_r^R \frac{\partial G}{\partial x_r} \tag{4.6}$$

where P and R are the set of all products, p, and reactants, r, respectively.

In addition to the reactions with other defects and bubbles, a new sink has been added to track growth of dislocations and their subsequent impact on point defect concentrations. A fixed concentration of single sized dislocations is introduced into the reacting defects. For a dislocation with size x, reacting with a interstitial with y uranium interstitials and z nitrogen interstitials, the dislocation grows by,

$$\text{dis}_x + \{y\text{U}_i : z\text{N}_i\} \rightleftharpoons \text{dis}_{x+y+z}. \tag{4.7}$$

A similar equation for vacancies is also possible, as well as for antisites:

$$\text{dis}_x + \{y\text{V}_\text{U} : z\text{V}_\text{N}\} \rightleftharpoons \text{dis}_{x-y-z}, \tag{4.8}$$

$$\text{dis}_x + \{\text{N}_\text{U} : y\text{V}_\text{U}\} \rightleftharpoons \text{dis}_{x-y}, \tag{4.9}$$

$$\text{dis}_x + \{\text{U}_\text{N} : z\text{V}_\text{N}\} \rightleftharpoons \text{dis}_{x-z}. \tag{4.10}$$

Dislocations are included similar to other defects via the FECD formulation, and is tracked via the number of atoms in a single dislocation, N_d:

$$\frac{\partial N_d}{\partial t} = \sum_i^I \frac{2\pi\eta_d Z_d}{\Omega \ln(R/r_d)} \rho (D_i + D_d) X_i F(f_d) G(r_d) \tag{4.11}$$

where I is the set of all defects interacting with the dislocation (i.e., vacancies, interstitials, and anti-sites), η_d is the value for which the dislocation grows or shrinks after reaction with a given defect (positive for interstitials, negative for vacancies, see Table 4.1), $Z_d = 100$ is the recombination factor to account for long-range attractions, similar to the $Z = 100$ used in all other reactions, D_i and D_d are the individual defect and dislocation diffusivities respectively, X_i

is the site fraction of interacting defect, F is the bracketed term in Eq. (4.5) which converts the driving force f_d into a reaction driver, and $G(r_d)$ is a suppressing function that terminates the dislocation growth once it reaches sizes similar to the grain boundary. The log term in Eq. (4.11) is a geometric factor for the rate of capture of cylindrical (line) sinks, and depends on the radius of the dislocation, r_d, and the equivalent volume of the line sink, R, which is dependent on the concentration of the lines. This term is an approximation of the toroidal capture volume of a line dislocation, and does not truly capture the ring structure of the dislocation loop, but it is a good first approximation. Since the log term is on the order of unity, and does not change much as R changes, this term is ignored in the current simulations. Finally, the reaction rate of each defect is the negative of Eq. (4.11), e.g., $\frac{\partial X_i}{\partial t} = -\frac{\partial N_d}{\partial t}$.

If the dislocations grow large enough, they will eventually reach the grain boundaries and be pinned. Any furter absorption by the dislocation will result in rapid diffusion of the defect to the grain boundary sink, effectively stopping growth of the dislocations. A termination function $G(r_d)$ is utilized in Eq. (4.11) that sets $\frac{\partial N_d}{\partial t} = 0$ once the dislocation size reaches the same size as the grain:

$$G(r_d) = \begin{cases} 1 & \text{if} \quad 2r_d < 2r_{grain} \\ 0 & \text{otherwise} \end{cases}. \tag{4.12}$$

where $2r_{grain} = 10\mu$m.

The reaction between dislocations and other defects is different in that their overall size grows rather than being consumed (or produced) via Eq. (4.5). Due to this, the driving force is much more complicated. The driving force for a reaction between defect i absorbed by a dislocation is formulated as,

$$f_d = -G_i^0 - k_B T \ln(X_i) + \frac{\partial G_{line}}{\partial n_d} + \frac{\partial G_{stoich}}{\partial n_d} + \frac{\partial G_{size}}{\partial n_d}, \tag{4.13}$$

where G_i^0 is the concentration-independent energy of the defect, the log term corresponds to the change in configurational entropy, and the last three G terms are the line energy, stoichiometric, and size energies respectively, which are formulated as the change in energy due to absorption (or emission) of a defect with a dislocation. Here, n_d is the number of atoms in a single dislocation, and is related to the atom fraction of all atoms in dislocations as $N_d = n_d c_d$, where c_d is the atom fraction of dislocations.

The energy of a dislocation loop can be reduced to a line energy, which is similar to the surface tension that acts on bubbles. The change in the energy as a function of length, $\frac{\partial G_{line}}{\partial l_d}$, has been estimated via several different methods, as discussed in Section 4.1, resulting in the line energy contribution to be calculated by,

$$\frac{\partial G_{line}}{\partial n_d} = \frac{\partial G_{line}}{\partial l_d}\frac{\partial l_d}{\partial N_d}\frac{\partial N_d}{\partial n_d} = \Omega^{1/3}\sqrt{\frac{\pi}{n_d}}\left(\frac{\partial G_{line}}{\partial l_d}\right), \tag{4.14}$$

where $l_d = 2\pi r_d$ is the circumference if a dislocation loop with radius r_d, and $\Omega = a_0^3/n_a$ is the volume consumed by a single defect, which is computed from the lattice parameter, a_0, and the number of atoms in the unit cell, n_a.

The distribution of uranium and nitrogen interstitial defects and their subsequent reaction rates with defects is not equal. However, unlike the UO_2 system where oxygen defects maintain their thermal equilibrium concentration at the temperatures of interest, and are assumed to move where needed, nitrogen in UN does not behave similarly. Given the growth of a dislocation, it is possible to preferentially absorb (or lose) one atom more than the other. To prevent an unphysical buildup of either uranium or nitrogen atoms at dislocations, a penalty is introduced by $\frac{\partial G_{stoich}}{\partial n_d}$ that will favor defects that keep the defect around perfect stoichiometry. For simplicity, a simple cubic forcing function is utilized,

$$\frac{\partial G_{stoich}}{\partial n_d} = 100\eta_{stoich}(\chi_d - 1)^3, \tag{4.15}$$

where χ_d is the ratio of nitrogen to uranium atoms in the dislocation. This value is tracked by applying the same reaction rate computed by Eq. (4.11) to χ_d along with a constant multiplier depending on the reacting defect, e.g., 1 for uranium vacancies and nitrogen interstitials, -1 for nitrogen vacancies and uranium interstitials, with higher constants for larger clusters.

Finally, the last energy term in Eq. (4.13) is utilized to prevent the dislocation shrinking to nonphysical sizes,

$$\frac{\partial G_{size}}{\partial n_d} = 10^6 \log(n_d^{min}/n_d)^3, \tag{4.16}$$

where n_d^{min} is the minimum number of atoms allowed in a dislocation. This formulation is somewhat artificial in that if a dislocation line gets too small, it will eventually annihilate due to the increasing line energy. However, this driving force addition prevents full destruction of the dislocations, and can be thought of as a nucleation term in that a concentration of small dislocations will always be present due to creation from bubble punching or shear stresses.

When running rate theory simulations of defects such as bubbles and dislocations, the population and size of the defects are both free variables. These values can be estimated by using a nucleation model, which requires an extensive knowledge of the birth of the particular defect. If no adequate nucleation model exists – as is the case for dislocations in nuclear fuel – either the concentration or defect size must be set, leaving one free variable free to capture the relative growth of the defects, either directly through the size or through an increase in concentration. In lieu of a nucleation model for dislocations, the fabrication dislocation line density for UC was utilized here was used as a guide $\rho = 5 \cdot 10^{13}$ [6]. In order to get dislocations to grow, a critical sized must be overcome – and thus a small enough line energy – to establish a regime of growth rather than annihilation. To capture this behavior, the number of atoms in the initial dislocations were estimated using a rough estimate for dislocation sizes that allowed growth:

$$\log(n_d^0) = T/100 - 7.5, \tag{4.17}$$

where T is temperature in [K], and n_d^0 is the number of atoms in each dislocation at the start of the simulation.

4.2.2 UN Centipede model

A Centipede simulation for uranium nitride fuel was recently published [23] and provided a first-of-a-kind simulation of irradiation enhanced self- and fission gas diffusion. Utilizing this model

Table 4.1: Atomistic data used for the Centipede modeling. H and S are either the formuation energy for the point defects, or the binding energy for the clusteres. Color coding of the values is used to signify the pedigree of data, for Good value, estimated from DFT, experiments, or crystal structure, Estimated value from MD that could use refinement, Estimated value from DFT that could use refinement and Undefined value with best guess. j_s, j_d, δ, and η_d are the jump sites, jump distance, degeneracy, and dislocation reaction factor respectively

Name	H [eV]	S [kB]	S_T [kB]	Q [eV]	w [THz]	j_s	j_d [Å]	δ	η_d
UN		-28.67	6						
N2		0.16	3.96						
Ui01:Ni00	0.00	-1.73	3	1.99	3.46	6	2.45	4	$1/2$
Ui00:Ni01	-1.69	-15.28	3	1.68	41.20	6	2.45	1	$1/2$
vU01:vN00	20.18	13.60	-3	3.27	8.71	12	3.46	1	$-1/2$
vU00:vN01	18.42	17.82	-3	3.14	13.90	12	3.46	1	$-1/2$
vU02:vN00	-0.64	27.73	-6	2.96	8.71	8	3.46	6	-1
vU00:vN02	-0.39	35.71	-6	2.84	13.80	8	3.46	6	-1
vU01:vN01	-0.70	31.18	-6	2.51	8.71	4	3.46	6	0
Un01:vN00	2.05	15.75	0		0.00		3.46	1	0
Un01:vN01	-0.82	33.57	-3	2.90	11.00	4	3.46	12	$-1/2$
Nu01:vU00	9.93	-2.18	0		0.00		3.46	1	0
Nu01:vU01	-2.76	11.41	-3	3.00	8.44	4	3.46	12	$-1/2$
Ui02:Ni00	-46.42	-3.46	6	1.99	3.46	6	2.45	8	1
Ui00:Ni02	-46.70	-30.56	6	1.68	41.20	6	2.45	3	1
Ui01:Ni01	-47.20	-17.01	6	1.99	3.46	6	2.45	16	1
Ui02:Ni01	-73.65	-18.74	9	1.99	3.46	6	2.45	8	$3/2$
Ui01:Ni02	-73.33	-32.29	9	1.99	3.46	6	2.45	8	$3/2$
Ui02:Ni02	-100.40	-34.02	9	1.99	3.46	6	2.45	8	2

as a starting point, both a number of improvements were introduced, including more refined atomistic data, and more complex reaction energies for the sink reactions.

Atomistic data

While exploring the larger interstitial clusters described in Section 4.1, all clusters were re-evaluated. This new data (Table 4.1) will be used here to maintain consistency with the values computed for the larger interstitial clusters, and is similar to previously calculated values. Color-coding is utilized in Table 4.1 to highlight where calculations remain to be completed. Of particular note is the lack of accurate data for the interstitial clusters, especially the activation barrier Q, which is estimated by utilizing the rate limiting mobility of each cluster constituent, i.e., either the uranium and nitrogen interstitial. In addition, the binding entropies for the larger interstitial clusters are selected to result in a zero total cluster entropy. In addition, a value of 2.5 eV per Å was utilized for the line energy based on the estimations outlined in Section 4.1.3.

Sink driving force updates

The driving force for the sink reactions, f_s (see f in Eq. (4.5) for implementation) has been updated to include two additional energy drivers, a stoichiometric term similar to that used for

Table 4.2: Constants for computing Eq. (4.19) taken from [62].

c_1	c_2	c_3	c_4	c_5	c_6	c_7
-1.033	3.372	-7.091	9.189	-5.858	1.950	-0.328

dislocations, and a term for bubble pressurization,

$$f_s = \Delta G_i^0 - k_B T \ln(X_i) + \frac{\partial G_{stoich}}{\partial n_i} + \frac{\partial G_{pressure}}{\partial n_i}. \tag{4.18}$$

The stoichiometric correction is the same as used for dislocations in Eq. (4.15), albeit is in relation to the reacting atom n_i. The bubble overpressurization term $\frac{\partial G_{pressure}}{\partial n_d}$ is adopted from previous work from Cooper et al. [23],

$$\frac{\partial G_{pressure}}{\partial n_d} = \sum_{i=2}^{9} (1-i) c_i \chi_b^{-i}, \tag{4.19}$$

where c_i is a set of constants fit from MD simulations and χ_b is the Schottky defect-to-xenon ratio in the bubbles. Table 4.2 displays the coefficients computed in [62]. Although the values were computed for UO_2, they are used as a first approximation and should be similar for uranium nitride.

Centipede simulations have typically consisted of the steady-state solution of defects rather than the time-evolution of the system. This resulted in calculations of diffusivities that were close to measured values. Since transient simulations are required for the dislocation growth model developed here, the bubble sink term must also grow in order to accurately mimic the behavior of the fuel. This results in a bubble sink term that looks like:

$$k_s = k_s^0 \begin{cases} \frac{B}{0.05}, & \text{if } B < 0.05, \\ 1, & \text{otherwise,} \end{cases} \tag{4.20}$$

where B is burnup in FIMA, and $k_s^0 = 4\pi < r_b c_b > Z_b$ is the steady state reaction coefficient for uranium nitride bubble sinks. Here, $Z_b = 100$ is the long-range capture radius of the bubble, and $< r_b c_b >= 10^{-3}$ [nm/nm^3] estimated from post irradiation examination.

In addition, the grain boundary sink strength is estimated using the values from [63]. For grain sizes on the order of 10 microns, the grain boundary sink strength is less than 10^{-4}, with some estimates around 10^{-7} [63]. To capture this slight sink concentration, 10^{-5} is used as a time-independent sink. This is especially important early in the simulation while the bubble sink strength is small, but is quickly overtaken by the bubble and dislocation sinks.

Updated point defect concentrations

Given the new data for uranium nitride clusters, Figs. 4.6 to 4.8 show the comparison between the old and new data at the so-called "mid" chemistry value, which traverses the middle of the UN phase space (see Fig. 3.6)

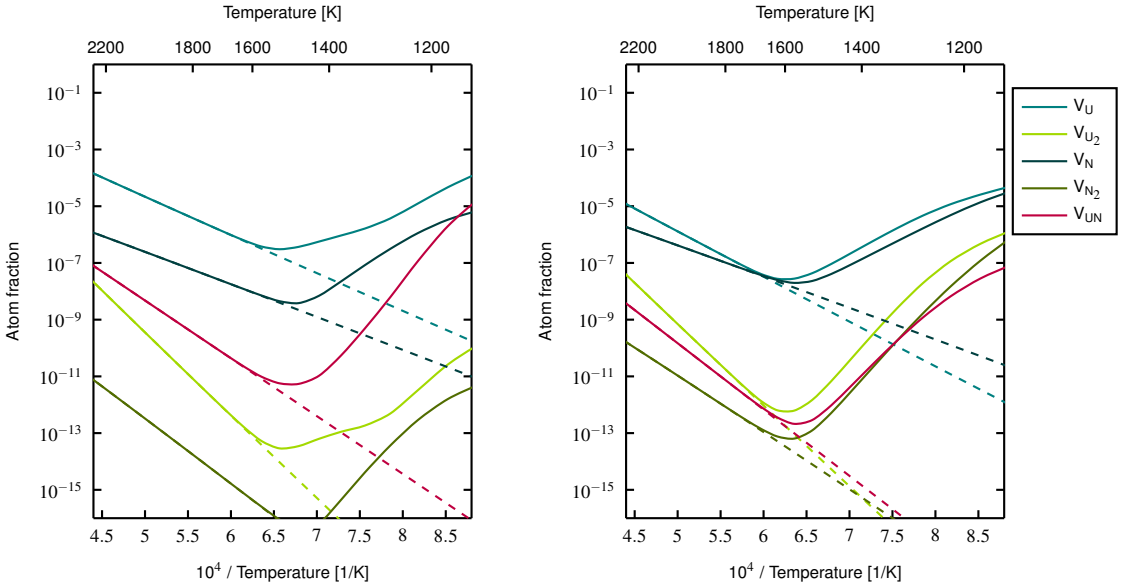

(a) Old data

(b) New data

Figure 4.6: Comparison of the irradiation enhanced concentration of vacancies between the old and new atomistic data for UN. The dashed lines correspond to the thermal equilibrium values, while the solid lines correspond to the irradiation enhanced values.

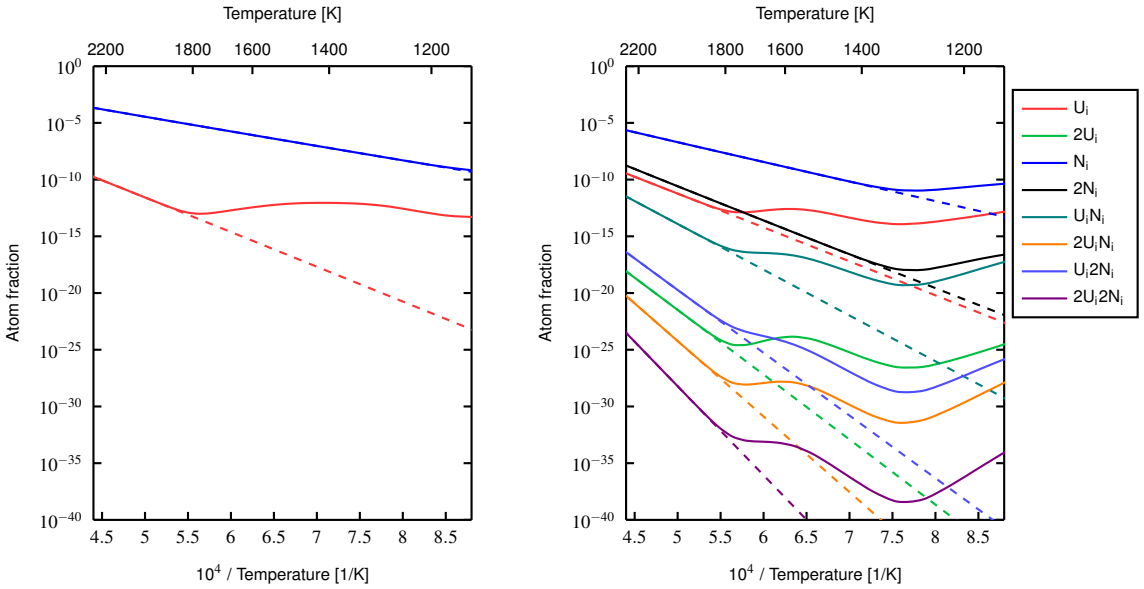

(a) Old data

(b) New data

Figure 4.7: Comparison of the irradiation enhanced concentration of interstitials between the old and new atomistic data for UN. Note the old data did not include the information for the larger clusters, so they are absent from the comparison in (a).

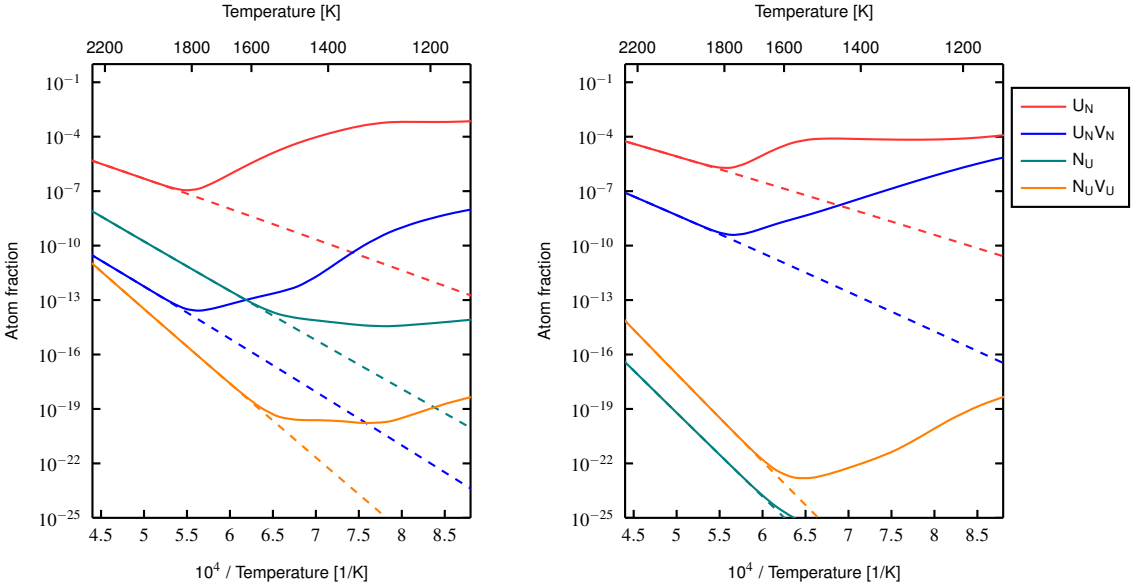

(a) Old data

(b) New data

Figure 4.8: Comparison of the irradiation enhanced concentration of antisites between the old and new atomistic data for UN. The dashed lines correspond to the thermal equilibrium values, while the solid lines correspond to the irradiation enhanced values.

4.2.3 New convergence criteria for transient simulations

Typically, Centipede simulations find the steady-state solution to this coupled set of ODEs, such that $\frac{dc_d}{dt} \leq \mathcal{R}$ for all defects, where $\mathcal{R}$ is the convergence criteria. Here, Centipede has been modified to track the evolution of clusters during irradiation. This new simulation capability was enabled by the new convergence criteria developed in MOOSE by the authors, and is an enabling feature to accurately capture the evolution of defects (and now dislocations) as a function of time.

Before introducing the new convergence criteria, the current methods utilized by MOOSE need to be discussed. In the unmodified version of MOOSE, two criteria are utilized during each timestep to ensure convergence in a transient simulation, named absolute and relative tolerance of the non-linear residuals, or `nl_abs_tol` and `nl_rel_tol` respectively. After each non-linear step, the L2-norm of all variable residuals are compared to these tolerances. The timestep is considered "converged" if this L2-norm is either less than the `nl_abs_tol` or is less than the L2-norm at the start of the timestep by `nl_rel_tol`. Several problems arise from these two convergence criteria. First, all variables are grouped together to a single absolute and relative tolerance, which allows for no refinement depending on the relevant physics. For example, an acceptable absolute tolerance for a thermo-mechanical simulation will be very different for either the temperature variables (which is typically solving for values on the order of thousands of degrees) and displacement variables (values on the order of 0.0001). Second, the relative tolerance is biased by the state of the system at the beginning of the timestep. For example, a poor estimate of the variable initial conditions could result in an extremely large initial residual,

for which a simple correction could lead to a drastically smaller residual, but still result in a solution that is far from convergence. Conversely, if the system is close to the physically correct solution, relative convergence could never be reached.

In an attempt to overcome these problems, a new "Problem" type `ReferenceResidualProblem` was introduced some years ago to modify the relative convergence criteria. This new method is used extensively in mechanics problems (e.g., fuel performance simulations in BISON), but still suffers from complexity and knowledge of the estimated residuals a priori. In `ReferenceResidualProblem`, the relative convergence criteria is modified to compare the L2-norm of the residual from a select set of kernels to a "reference". The compared L2-norm residual is accumulated via the tagging system, and requires manually enabling residual accumulation from kernels in the input file. The "reference" is a selected residual contribution that is not included in the L2-norm summation, and is typically selected as the boundary conditions of the problem. In addition to using the relative tolerance to compare against a physical value of the system, `ReferenceResidualProblem` also separates the contributions from each variable, allowing each variable to be compared against itself. Once the L2-norm of the selected residuals is less than the "reference" value for each variable by `nl_rel_tol`, then the timestep is considered converged. Note, the absolute tolerance criteria is not modified, and is allowed to operate simultaneously from this adopted relative convergence criteria.

While `ReferenceResidualProblem` has been useful for situations where the selection of the "reference" value is easy, it still suffers from a couple of problems, namely, if boundary conditions are not utilized (e.g., stress-free strain from thermal expansion of floating parts or, perhaps more relevant, cluster dynamics simulations) or if the correct "reference" varies as a function of time.

To illustrate the need for a new convergence criteria, lets take a single particle problem, starting with two springs, one attached to a wall and one being pulled as in Fig. 4.9a. Static equilibrium is set by the balancing of the forces of two springs on the particle, with equal but opposite signs, with the displacement of the particle as the free variable. Absolute tolerance would work well here as a convergence option, with the tolerance set to something like 10^{-6} times the force of one of the springs on the particle.

Next, place two more weak springs as in Fig. 4.9b, introducing a new free variable as displacement in the y-direction. In this case, absolute tolerance will not work well when drastically different forces are acting for different variables. The standard grouped absolute tolerance criteria would work if the forces were always about the same for all time and both directions. This method would not be applicable if the springs in the x-direction were much stiffer than in the y-direction, or if the spring stiffness changed as a function of time. A single fixed absolute tolerance will either be too loose, resulting in unconverged solutions, or too tight, resulting in an ability to complete the simulation.

As discussed before, the "reference" is typically built by applying `extra_vector_tags` to everything but the boundary conditions. For example, the reference residual would be identical to the actual residual for the case where there are four springs and no boundary conditions, as in Fig. 4.9c. In such a simple case, you could select one force in each direction to build an appropriate reference residual, but things are not always so simple. For example, consider Fig. 4.9d in which the springs now act in different dimsions, and could even vary with time.

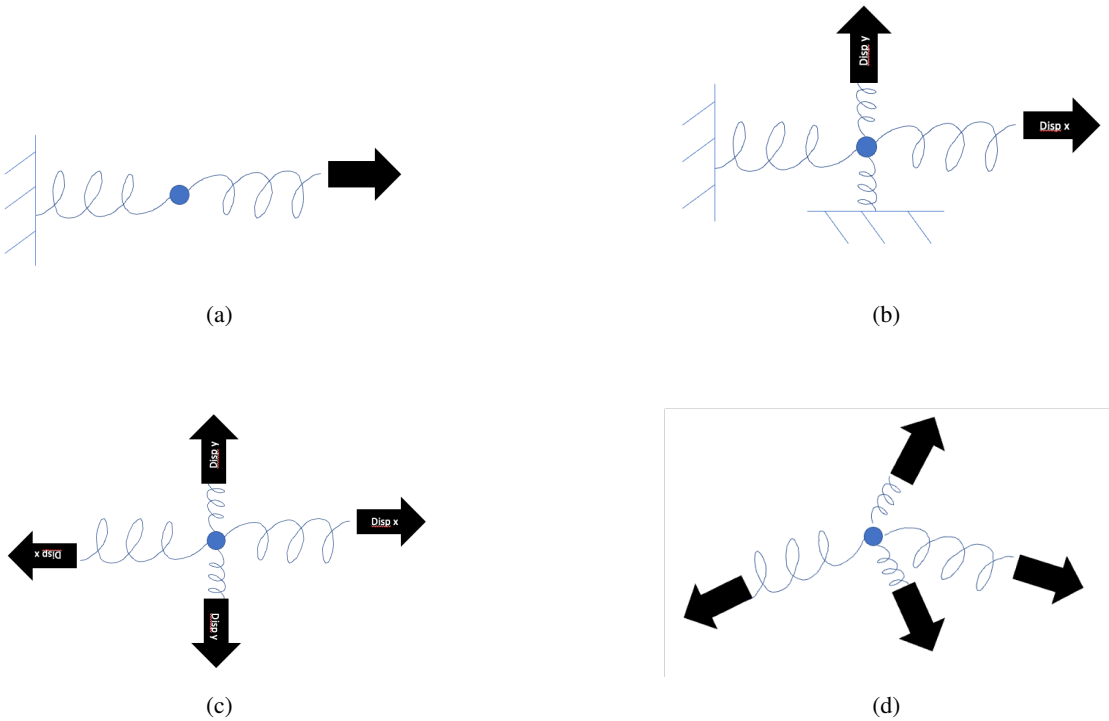

(a) (b)

(c) (d)

Figure 4.9: Examples that highlight the different options for convergence criteria using a single particle and springs.

At the suggestion of a colleague at Idaho National Laboratory, Ben Spencer, `ReferenceResidualProblem` has been modified to remove the need to set the "reference," and instead uses the summation of the absolute value of all contributions to each variables residual as the "reference". By supplying `reference_vector = aref` to all kernels, boundary conditions, and constraints via the `GlobalParams` block, the built-in MOOSE tagging system now automatically compiles the absolute values of the residual contributions, performs a variable-specific L2-norm, and then uses the newly computed value to check for convergence of each timestep.

Enabled by this new convergence criteria, transient simulations in Centipede are now possible, a key requirement to capture the evolution of dislocations.

4.3 Dislocation Simulation Results

Combining the new data, time dependent sink terms, dislocation model, and new convergence criteria discussed in the previous sections, the total evolution of dislocations as a function of time and burnup is shown in Fig. 4.10. The first thing to note is that the the dislocation line density at high burnups is larger for the intermediate temperatures (1400 K). This is clearly visible in Fig. 4.11, with the solid line showing the dislocation line density as a function of temperature at 6.8% FIMA. The behavior is due to the total dislocation content saturates at lower and lower dislocation line densities as a function of time, a consequence of the formulation size limit of the dislocation set to the grain size. Eventually, the dislocation content does not grow larger than the original fabrication dislocation density above 1600 K.

Figure 4.12 shows the dislocation growth compared to measured values from UC and UO_2. With both data sets, there seems to be an incubation time before the dislocation starts to grown, while the simulation shows that growth of the dislocation line density is rapid in the first few stages of irradiation. This delayed dislocation growth indicates there is more complexity to the dislocation nucleation than the simple model utilized here, warranting more work in getting the initial dislocation size and concentrations correct. If the model is shifted to the right by 3% FIMA, the data closely resembles the measured values for UC. It is important to note that the experimental values indicate an almost exactly linear relationship for dislocation line density, while the model resembles more of a square-root dependence in growth. Even more complicating is the slightly exponential growth measured for UO_2. A nucleation model that more accurately reflects the initial dislocation sizes may be able to capture the more linear behavior observed in UC. If this same 3% FIMA shift is carried over to the comparison with the Centipede model with the dislocation content as a function of temperature, the comparison to data is also more favorable, shown in the dashed line in Fig. 4.11.

4.4 Discussion and future work

The DFT calculations shown here provide valuable insight into how interstitials form and interact in uranium nitride. Pictures such as those in Fig. 4.3 not only allow visual aids for development of Centipede and BISON level models, but can simultaneously be used to extract energies of the dislocations, as was done here to provide an estimate of the line energy. The immediate

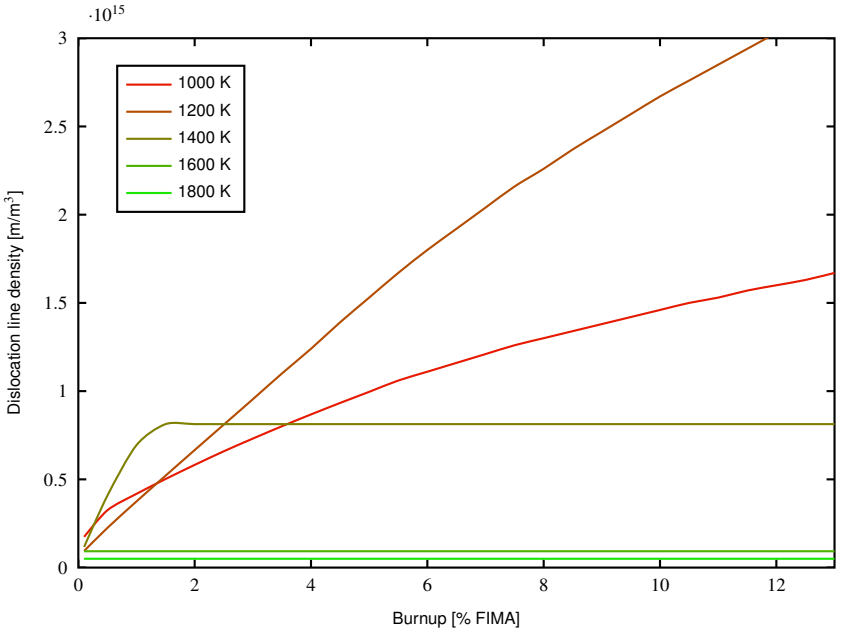

Figure 4.10: Line density of dislocations as a function of time.

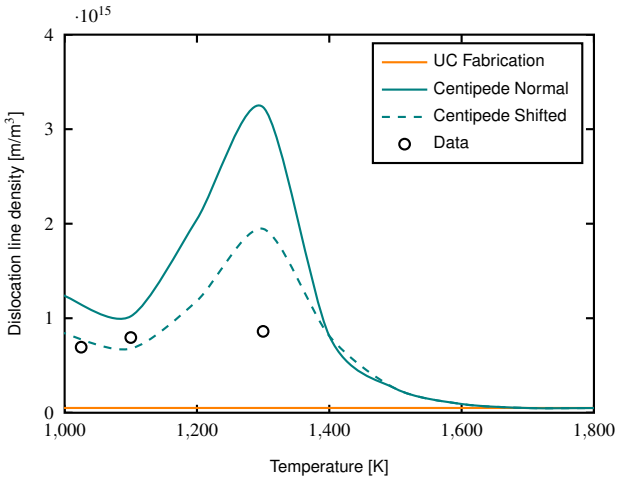

Figure 4.11: Line density of dislocations at 6.8% FIMA.

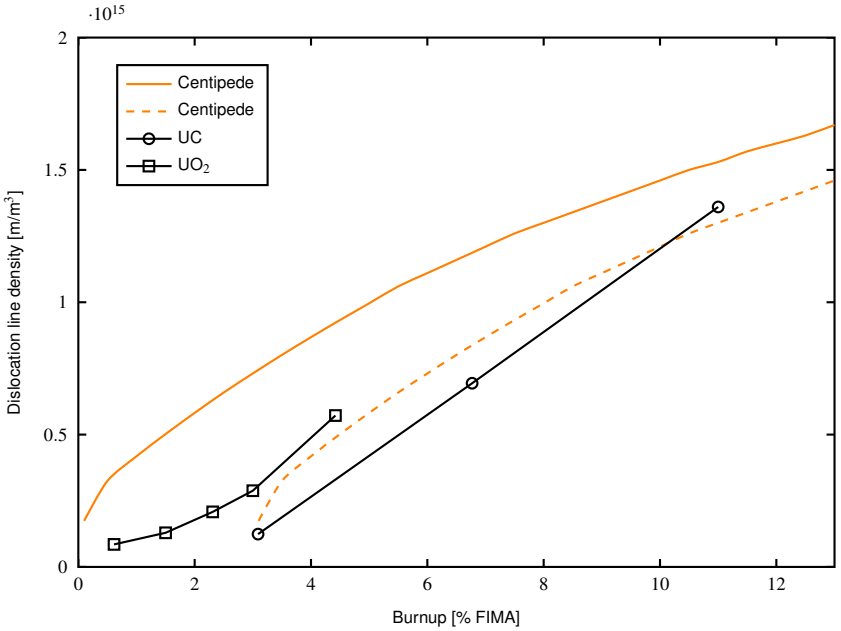

Figure 4.12: Line dislocations at 1025K compared to data. The dashed line corresponds to a 3 % FIMA shift to account for the incubation time present in the data. Also included is data from UC [6] and UO_2 [34].

next-step is the modeling of $\{110\}$ cluster growth in the orthogonal 100 direction. These calculations should in principle produce actual interstitial loops as the clusters will form partial $\{110\}$ planes.

It is uncertain whether DFT calculations alone will be able to provide accurate data on the dislocation line energies, due to the severe system size limitations. However, the energetics of the clusters obtained from DFT can also be used to improve the parametrization of empirical potentials. Therefore, the continuation of this task may involve molecular dynamics simulations, in order to provide more useful data to the fission gas model (while ensuring the accuracy of such simulations by comparing key results with ab-initio).

The DFT calculations helped fill out the energies of the larger interstitial clusters. Ultimately, temperature-dependent entropies are necessary to capture the full energy of the defect, especially under irradiation where the primary defect driving diffusivity may transition. Unfortunately, accurately tracking these larger clusters using DFT is tedious, and require careful sampling of all possible defect configurations. The energetics of the interstitial clusters will continue to be pursued, especially the binding enthalpies of larger clusters, and activation energies and entropies of the smaller more numerous interstitial clusters. As the Centipede dislocation and BISON fission gas release and swelling models are more refined, continuing communication on the atomistic data needs is essential to ensure the important defect space is available for use, while simultaneously avoiding refinement of data that is ultimately unnecessary.

The dislocation model discussed here is very simple in nature, while following the FECD formulation of traditional Centipede calculations. This model benefits from the natural incor-

poration of ab initio data, but likely suffers from an oversimplification on the nucleation of the defects. Unfortuntely, such models are extremely difficult to quantitatively capture, although the simulations here may provide some insight; the change in the defect energies as a function of temperature require an exponential increase in initial dislocation size in order to ensure the dislocations do not shrink and ultimately annihilate. The model prevents this in two ways. The first is the energtic term defined in Eq. (4.16) that prevents dislocations from shrinking below a critical size. The second is the ad hoc initial concentration of atoms per dislocation defined in Eq. (4.17), while maintaining the initial dislocation line density constant across all temperatures. While these simplifications allow the simulations to capture the expected dislocation growth, they are likely oversimplistic, and could benefit from a more physical formulation.

Despite the many simplifications in the dislocation model, the overall peaking of the dislocation line density around 1300 K mimics very closely the breakaway swelling that occurs at similar temperatures in UC and UN. Surprisingly, the peak corresponds more closely to the swelling peak observed in carbide fuel than that of nitride fuel, which occurs at about 200 K higher temperatures. This again points to deficiencies in the nucleation model utilized here, but the indication of the peak shows promise in ability of the mechanistic dislocation model to supply the necessary behavior to enable breakaway swelling in a BISON fission gas swelling and release model.

5 Conclusions

Based on previous modeling work [4,10], a dislocation bubble model was implemented in Sifgrs and was applied to UN. This model successfully captures the breakaway swelling phenomenon seen in nitride fuel by allowing the gas to concentrate in dislocation bubbles at higher temperatures as opposed to bulk bubbles at lower temperatures. This success is dependent on an empirical dislocation density function that will eventually be replaced by a mechanistic model.

Analysis of experimental data and the results of this modeling work produced the following useful conclusions:

- Bubbles nucleate along dislocation lines at a constant rate of roughly 10^6 bubbles/m, independent of temperature.
- The quasi-stationary approximation is not always valid for UN.
- Bubble pressures do not appear to exceed the dislocation loop punching threshold.
- The coverage of dislocation lines by bubbles remains below 20% and is insufficient for bubble interconnection to the point of gas release.
- Some fraction of the bulk bubbles at low temperature may have been too small to be measured, but still contribute to the microscopic swelling.

While the JOYO assessment case yielded fairly decent results, the SP1 assessment demonstrated that the dislocation bubbles are trapping too much of the fission gas at high temperatures greater than $\sim$1700 K. This issue could be remedied by a mechanistic dislocation model showing less dislocation density at higher temperatures.

Early ab-initio results suggest that the most favorable arrangement of interstitial clusters is in the $\{110\}$ orientation, and that the binding energy of the cluster increases when U or N interstitials are captured at one of the extremities along the $\{110\}$ axis. We also observe a striking resemblance between the lowest-energy configurations of these clusters, and the structure of a $\langle 110 \rangle$ dislocation loop, which suggests that a dislocation loop could nucleate from these clusters. So far, DFT results do not allow the description of an actual interstitial loop. Our immediate perspective is to calculate the growth potential of these clusters in the $\{100\}$ direction orthogonal to the $\{110\}$ axis of the clusters, in order to form a partial interstitial plane, equivalent to a dislocation loop. Also, we have calculated from DFT the excess of energy of the clusters compared to an ideal lattice containing the same number of atoms. It appears that the energy obtained as a function of the clusters length is of the same order as the dislocation energy obtained from elastic theory (which itself is of the same order as literature results on UO_2). Although these quantities are not equivalent, once DFT clusters will be extended enough to model an actual dislocation loop, the asymptotic value of the excess energy should in principle become equivalent to a line energy.

Acknowledgements

This work was sponsored by the Office of Nuclear Energy, Nuclear Energy Advanced Modeling and Simulation (NEAMS) program, as well as the Office Nuclear Energy Fuel Cycle Research and Development program. Los Alamos National Laboratory, an affirmative action/equal opportunity employer, is operated by Triad National Security, LLC, for the National Nuclear Security Administration of the U.S. Department of Energy under Contract No. 89233218CNA000001. Accordingly, the U.S. Government retains a non-exclusive, royalty free license to publish or reproduce the published form of this contribution, or allow others to do so, for U.S. Government purposes.

Bibliography

[1] T. Preusser, Modeling of Carbide Fuel Rods, Nuclear Technology 57 (3) (1982) 343–371.

[2] E. Storms, An Equation Which Describes Fission Gas Release from UN Reactor Fuel, Journal of Nuclear Materials 158 (C) (1988) 119–129.

[3] J. Rest, M. Cooper, J. Spino, J. Turnbull, P. Van Uffelen, C. Walker, Fission gas release from UO2 nuclear fuel: A review, Journal of Nuclear Materials 513 (2019) 310–345. doi:https://doi.org/10.1016/j.jnucmat.2018.08.019.
URL https://www.sciencedirect.com/science/article/pii/S0022311518309449

[4] T. Barani, G. Pastore, A. Magni, D. Pizzocri, P. Van Uffelen, L. Luzzi, Modeling intragranular fission gas bubble evolution and coarsening in uranium dioxide during in-pile transients, Journal of Nuclear Materials 538 (2020) 152195.

[5] S. T. Murphy, P. Fossati, R. W. Grimes, Xe diffusion and bubble nucleation around edge dislocations in UO2, Journal of Nuclear Materials 466 (2015) 634–637.

[6] I. Ray, H. Blank, Microstructure and fission gas bubbles in irradiated mixed carbide fuels at 2 to 11 a/o burnup, Journal of Nuclear Materials 124 (1984) 159–174.

[7] C. Baker, The fission gas bubble distribution in uranium dioxide from high temperature irradiated sghwr fuel pins, Journal of Nuclear Materials 66 (3) (1977) 283–291. doi:https://doi.org/10.1016/0022-3115(77)90117-9.

[8] P. Lösönen, On the behaviour of intragranular fission gas in UO2 fuel, Journal of Nuclear Materials 280 (1) (2000) 56–72. doi:https://doi.org/10.1016/S0022-3115(00)00028-3.

[9] H. Matzke, Science of Advanced LMFBR Fuels, Elsevier Science Pub. Co. Inc.,New York, NY, United States, 1986.

[10] C. Matthews, J. Rizk, C. Galvin, M. Cooper, D. Andersson, Fission Gas Models for UN Fuels in Bison, Tech. rep., Los Alamos National Laboratory (2022).

[11] G. Pastore, D. Pizzocri, C. Rabiti, T. Barani, P. Van Uffelen, L. Luzzi, An effective numerical algorithm for intra-granular fission gas release during non-equilibrium trapping and resolution, Journal of Nuclear Materials 509 (2018) 687–699.

[12] M. Colin, M. Coquerelle, I. Ray, C. Ronchi, C. Walker, H. Blank, The Sodium-Bonding Pin Concept for Advanced Fuels Part I: Swelling of Carbide Fuel up to 12% Burnup, Nuclear Technology 63 (3) (1983) 442–460.

[13] H. Blank, Nonoxide Ceramic Nuclear Fuels (2006).

[14] C. Ronchi, I. Ray, H. Thiele, J. van de Laar, Swelling analysis of highly-rated MX-type LMFBR fuels: II. Microsopic swelling behaviour, Journal of nuclear materials 74 (2) (1978) 193–211.

[15] U. Benedict, G. Giacchetti, H. Matzke, K. Richter, C. Sari, H. E. Schmidt, Study of Uranium-Plutonium Carbide-Based Fuel Simulating High Burnup, Nuclear technology 35 (1) (1977) 154–161.

[16] C. Matthews, R. Perriot, M. W. Cooper, C. R. Stanek, D. A. Andersson, Cluster dynamics simulation of uranium self-diffusion during irradiation in uo2, Journal of Nuclear Materials 527 (C) (2019) 151787.

[17] C. Matthews, R. Perriot, M. Cooper, C. R. Stanek, D. A. Andersson, Cluster dynamics simulation of xenon diffusion during irradiation in uo2, Journal of Nuclear Materials 540 (2020) 152326.

[18] M. Cooper, K. Gamble, L. Capolungo, C. Matthews, D. Andersson, B. Beeler, C. Stanek, K. Metzger, Irradiation-enhanced diffusion and diffusion-limited creep in u3si2, Journal of Nuclear Materials 555 (2021) 153129.

[19] X.-Y. Liu, C. Matthews, W. Jiang, M. Cooper, J. Hales, D. Andersson, Atomistic and cluster dynamics modeling of fission gas (xe) diffusivity in triso fuel kernels, Journal of Nuclear Materials 561 (2022) 153539.

[20] J. Turnbull, C. Friskney, J. Findlay, F. Johnson, A. Walter, The diffusion coefficients of gaseous and volatile species during the irradiation of uranium dioxide, Journal of Nuclear Materials 107 (2) (1982) 168–184.

[21] D. Andersson, P. Garcia, X.-Y. Liu, G. Pastore, M. Tonks, P. Millett, B. Dorado, D. Gaston, D. Andrs, R. Williamson, R. Martineau, B. Uberuaga, C. Stanek, Atomistic modeling of intrinsic and radiation-enhanced fission gas (xe) diffusion in uo2±x: Implications for nuclear fuel performance modeling, Journal of Nuclear Materials 451 (1) (2014) 225–242.

[22] K. Gamble, G. Pastore, M. Cooper, D. Andersson, C. Matthews, B. Beeler, L. Aagesen, T. Barani, D. Pizzocri, Improvement of the bison u3si2 modeling capabilities based on multiscale developments to modeling fission gas behavior, Journal of Nuclear Materials 555 (2021) 153097.

[23] M. W. D. Cooper, J. Rizk, C. Matthews, V. Kocevski, G. Graven, D. A. Andersson, Simulations of the defect concentrations and diffusivity of U, N and Xe in uranium mononitride under thermal equilibrium and irradiation conditions, Journal of Nuclear Materials– In review (2023).

[24] D. Pizzocri, G. Pastore, T. Barani, A. Magni, L. Luzzi, P. Van Uffelen, S. Pitts, A. Alfonsi, J. Hales, A model describing intra-granular fission gas behaviour in oxide fuel for advanced engineering tools, Journal of Nuclear Materials 502 (2018) 323–330.

[25] T. Barani, G. Pastore, D. Pizzocri, D. Andersson, C. Matthews, A. Alfonsi, K. Gamble, P. Van Uffelen, L. Luzzi, J. Hales, Multiscale modeling of fission gas behavior in u3si2 under lwr conditions, Journal of Nuclear Materials 522 (2019) 97–110.

[26] D. Olander, D. Wongsawaeng, Re-solution of fission gas – A review: Part I. Intragranular bubbles, Journal of Nuclear Materials 354 (1) (2006) 94–109.

[27] C. Matthews, D. Schwen, A. C. Klein, Radiation re-solution of fission gas in non-oxide nuclear fuel, Journal of Nuclear Materials 457 (2015) 273–278.

[28] C. Matthews, D. A. Andersson, C. Unal, Radiation Re-solution Calculation in Uranium-Silicide Fuels, Tech. Rep. LA-UR-16-22099, Los Alamos National Laboratory (2016).

[29] Z.-G. Mei, B. Ye, A. M. Yacout, B. Beeler, Y. Gao, First-principles study of the surface properties of uranium carbides, Journal of Nuclear Materials 542 (2020) 152257.

[30] D. Bocharov, First principles simulations on surface properties and reactivity of sustainable nitride nuclear fuels, Ph.D. thesis, University of Latvia (2012).

[31] S. Torquato, Nearest-neighbor statistics for packings of hard spheres and disks 51 (4) (1995) 3170–3182.

[32] D. Pizzocri, C. Rabiti, L. Luzzi, T. Barani, P. Van Uffelen, G. Pastore, Polypole-1: An accurate numerical algorithm for intra-granular fission gas release, Journal of Nuclear Materials 478 (2016) 333–342.

[33] M. V. Speight, A calculation on the migration of fission gas in material exhibiting precipitation and re-solution of gas atoms under irradiation, Nuclear Science and Engineering 37 (2) (1969) 180–185.

[34] K. Nogita, K. Une, Radiation-induced microstructural change in high burnup UO2 fuel pellets, Nuclear Instruments and Methods in Physics Research Section B: Beam Interactions with Materials and Atoms 91 (1) (1994) 301–306.

[35] T. Kogai, Modelling of fission gas release and gaseous swelling of light water reactor fuels, Journal of Nuclear Materials 244 (2) (1997) 131–140.

[36] J. L. ROUTBORT, H. MATZKE, Grain-boundary diffusion of u in pure and doped uranium carbides with different c/u ratios, Journal of the American Ceramics Society 58 (3-4) (1975) 81–84.

[37] K. D. Johnson, D. A. Lopes, Grain growth in uranium nitride prepared by spark plasma sintering, Journal of Nuclear Materials 503 (2018) 75–80.

[38] R. White, The development of grain-face porosity in irradiated oxide fuel, Journal of Nuclear Materials 325 (1) (2004) 61–77.

[39] K. Tanaka, K. Maeda, K. Katsuyama, M. Inoue, T. Iwai, Y. Arai, Fission gas release and swelling in uranium–plutonium mixed nitride fuels, Journal of Nuclear Materials 327 (2) (2004) 77–87.

[40] Y. Arai, S. Fukushima, K. Shiozawa, M. Handa, Fabrication of (u, pu)n fuel pellets, Journal of Nuclear Materials 168 (3) (1989) 280–289.

[41] M. Cooper, C. Matthews, D. Andersson, Development of bubble evolution model for new mechanistic transient fission gas release capability in BISON, Tech. rep., Los Alamos National Laboratory (2023).

[42] N. Bertin, L. Capolungo, A fft-based formulation for discrete dislocation dynamics in heterogeneous media, Journal of Computational Physics 355 (2018) 366–384. doi:https://doi.org/10.1016/j.jcp.2017.11.020.
URL https://www.sciencedirect.com/science/article/pii/S0021999117308586

[43] M. Verdier, M. Fivel, I. Groma, Mesoscopic scale simulation of dislocation dynamics in fcc metals: Principles and applications, Modelling and Simulation in Materials Science and Engineering 6 (6) (1998) 755. doi:10.1088/0965-0393/6/6/007.
URL https://dx.doi.org/10.1088/0965-0393/6/6/007

[44] R. Santos-Güemes, B. Bellón, G. Esteban-Manzanares, J. Segurado, L. Capolungo, J. LLorca, Multiscale modelling of precipitation hardening in al–cu alloys: Dislocation dynamics simulations and experimental validation, Acta Materialia 188 (2020) 475–485. doi:https://doi.org/10.1016/j.actamat.2020.02.019.
URL https://www.sciencedirect.com/science/article/pii/S1359645420301233

[45] S. Kashibe, K. Une, K. Nogita, Formation and growth of intragranular fission gas bubbles in UO2 fuels with burnup of 6–83 GWd/t, Journal of Nuclear Materials 206 (1) (1993) 22–34. doi:10.1016/0022-3115(93)90229-R.

[46] M. Veshchunov, V. Ozrin, V. Shestak, V. Tarasov, R. Dubourg, G. Nicaise, Development of the mechanistic code MFPR for modelling fission-product release from irradiated UO2 fuel, Nuclear Engineering and Design 236 (2) (2006) 179–200. doi:10.1016/j.nucengdes.2005.08.006.

[47] K. Nogita, K. Une, Radiation-induced microstructural change in high burnup UO2 fuel pellets, Nuclear Instruments and Methods in Physics Research Section B: Beam Interactions with Materials and Atoms 91 (1-4) (1994) 301–306. doi:10.1016/0168-583X(94)96235-9.

[48] M. Veshchunov, V. Shestak, Model for evolution of crystal defects in UO2 under irradiation up to high burn-ups, Journal of Nuclear Materials 384 (1) (2009) 12–18. doi:10.1016/j.jnucmat.2008.09.024.

[49] K. E. Bloechl, Projector augmented-wave method, Physical Review B 50 (1994) 17953.

[50] G. Kresse, J. Joubert, From ultrasoft pseudopotentials to the projector augmented-wave method, Physical Review B 59 (1999) 1758.

[51] G. Kresse, J. Hafner, Ab initio molecular dynamics for liquid metals, Physical Review B 47 (1993) 558.

[52] G. Kresse, J. Furthmueller, Efficiency of ab-initio total energy calculations for metals and semiconductors using a plane-wave basis set, Computational Materials Science 6 (1996) 15.

[53] G. Kresse, J. Furthmueller, Efficient iterative schemes for ab initio total-energy calculations using a plane-wave basis set, Physical Review B 54 (1996) 11169.

[54] J. P. Perdew, K. Burke, M. Ernzerhof, Generalized gradient approximation made simple, Physical Review Letters 77 (1999) 3865.

[55] V. Kocevski, D. A. Rehn, M. W. Cooper, D. A. Andersson, First-principles investigation of uranium mononitride (un): Effect of magnetic ordering, spin-orbit interactions and exchange correlation functional, Journal of Nuclear Materials 559 (2022) 153401.

[56] V. Kocevski, M. W. Cooper, A. J. Claisse, D. A. Andersson, Development and application of a uranium mononitride (UN) potential: Thermomechanical properties and Xe diffusion, Journal of Nuclear Materials 562 (2022) 153553. doi:10.1016/j.jnucmat.2022.153553.
URL https://linkinghub.elsevier.com/retrieve/pii/S0022311522000496

[57] A. Kuksin, S. Starikov, D. Smirnova, V. Tseplyaev, The diffusion of point defects in uranium mononitride: Combination of DFT and atomistic simulation with novel potential, Journal of Alloys and Compounds 658 (2016) 385–394. doi:10.1016/j.jallcom.2015.10.223.

[58] P. Xiu, M. Jin, K. Bawane, B. Tyburska-Pueschel, B. Jaques, K. Field, J. Giglio, L. He, Dislocation loops in proton irradiated uranium-nitrogen-oxygen system, Journal of Nuclear Materials 557 (2021) 153244.

[59] D. Trinkle, Energy of a dislocation, http://dtrinkle.matse.illinois.edu/MatSE584/kap_5/backbone/r5_2_3.html, accessed: 2023-07-31.

[60] D. Parfitt, C. Bishop, M. Wenman, R. Grimes, Strain fields and line energies of dislocations in uranium dioxide, Journal of Physics: Condensed Matter 22 (2010) 175004.

[61] S. L. Hayes, J. K. Thomas., K. L. Peddicord, Material property correlations for uranium mononitride, Journal of Nuclear Materials 171 (1990) 271–288.

[62] M. W. D. Cooper, C. Matthews, A. D. R. Andersson, Investigating bubble pressures in irradiated UO2 for understanding fragmentation of high burnup structure-doi:10.2172/1773295.
URL https://www.osti.gov/biblio/1773295

[63] A. D. Brailsford, R. Bullough, The theory of sink strengths, Philosophical Transactions of the Royal Society of London. Series A, Mathematical and Physical Sciences 302 (1465) (1981) 87–137. doi:10.1098/rsta.1981.0158.